NUMERICAL DISPERSION IN NON-HYDROSTATIC MODELING OF LONG-WAVE PROPAGATION

A DISSERTATION SUBMITTED TO THE GRADUATION DIVISION OF THE UNIVERSITY OF HAWAIʻI AT MĀNOA IN PARTIAL FULFILLMENT OF THE REQUIREMENTS FOR THE DEGREE OF

DOCTOR OF PHILOSOPHY

IN

OCEAN AND RESOURCES ENGINEERING

AUGUST 2018

By

Linyan Li

Dissertation Committee:

Kwok Fai Cheung, Chairperson

Gerard J. Fryer

Zhenhua Huang

Eva-Marie Nosal

Albert S. Kim

Acknowledgements

Six years ago, I received an offer letter from Dr. Kwok Fai Cheung and got the opportunity to come to Hawaii. I embarked on a new journey, filled with good times to enjoy and trials to overcome. Throughout this journey, Dr. Cheung is one of the persons who has changed my life. I would like to thank him for all the support he gives. His continuing support through funding from his grants and contracts over these years has enabled me to stay and finish this program. His professional guidance has opened my mind and broadened my knowledge in both the scientific and engineering world. He is patient and forgiving when progress in the work is slow, and I make mistakes. He always respects me as a student and encourages me to voice my own opinions and thoughts. His help has led me to succeed thus far, and his example of being a teacher and professor will guide me forever.

I am also deeply appreciative of my committee member's support and input. Dr. Albert Kim provided insightful comments on the mathematical derivation of the numerical dispersion relations. Dr. Eva-Marie Nosal gave valuable input on the solution of the numerical experiments. Dr. Zhenhua Huang provided very helpful discussions during my comprehensive exam. Dr. Gerard Fryer shared a lot of his deep thoughts on seismology and geology.

I have the privilege of working with Dr. Han Yue (currently at Peking University) and Dr. Thorne Lay of the University of California Santa Cruz on earthquake source studies. Their broad knowledge and unique insights on seismology have significantly improved the quality of this research. I would also like to thank some very special ORE researchers, who helped me a lot over these years: Dr. Ning Li, Dr. Yeifei Bai, Dr. Yoshiki Yamazaki, Troy Heitmann, and Conghao Xu. Their friendship, insightful input

Abstract

Numerical discretization with a finite-difference scheme is known to introduce truncation errors in the form of frequency dispersion in depth-integrated models commonly used in tsunami research and hazard mapping. While prior studies on numerical dispersion have focused on the shallow-water equations, we include the depth-integrated non-hydrostatic pressure and vertical velocity through a Keller box scheme and investigate the properties of the resulting system. Fourier analysis of the discretized governing equations gives rise to a dispersion relation in terms of the time step, grid size, and wave direction. The interworking of the dispersion relation is elucidated by its lead-order approximation, one and two-dimensional numerical experiments, and a case study of the tsunami generated by the 2010 Mentawai Mw 7.8 earthquake.

The dispersion relation, aided by its lead-order approximation from the Taylor series expansion, shows that coupling between the spatial discretization and non-hydrostatic terms results in significant reduction of numerical dispersion outside the shallow-water range. The time step, which counteracts numerical dispersion from spatial discretization, only has secondary effects within the applicable range of Courant numbers. Numerical dispersion also decreases for wave propagation oblique to the principal axes of the grid due to effective increase in spatial resolution. A numerical flume experiment of standing waves indicates minor contributions from the implicit solution scheme of the non-hydrostatic terms. A second numerical experiment verifies the properties deduced from the analytical results and demonstrates the effectiveness of discretization in altering progressive waves over a two-dimensional grid. The computational results also demonstrate generation of spurious, short-period trailing waves from hydrostatic model with insufficient numerical dispersion. Since the governing equations for the non-

hydrostatic system trend to underestimate dispersion in shoaling water, the numerical effects are complementary in producing a solution closer to Airy wave theory.

A case study of the 2010 Mentawai *Mw* 7.8 earthquake and tsunami event, which has a compact source adjacent to a deep trench, demonstrates the role of dispersion in wave propagation and the implications for the commonly-used source inversion techniques. Non-dispersive models are often used with an initial static sea-surface pulse derived from seafloor deformation in computation of tsunami Green's functions. We compare this conventional approach with more advanced techniques, which use Green's functions computed by a dispersive model with an initial static sea-surface pulse and with the surface waves generated from kinematic seafloor deformation. The fine subfaults needed to resolve the compact rupture results in dispersive waves that require a non-hydrostatic model. The Green's functions from the hydrostatic model are overwhelmed by spurious, grid-dependent short-period oscillations, which are filtered prior to their application. These three sets of tsunami Green's functions are implemented in finite-fault inversions with and without seismic and geodetic data. Seafloor excitation and wave dispersion produce more spread-out waveforms in the Green's functions leading to larger slip with more compact distribution through the inversions. If the hydrostatic Green's functions are not filtered, the resulting slip spreads over a large area to eliminate the numerical artifacts from the lack of dispersion. The fit to the recorded tsunami and the deduced seismic moment, which reflects the displaced water volume, is relatively insensitive to the approach used for computing Green's functions.

Table of Contents

List of Figures

Chapter 1
Introduction

Numerical long-wave models have long been an essential tool for tsunami research and flood hazard mapping. Conventional non-dispersive models, based on finite-difference solution of the shallow-water equations, have been widely used due to their simple numerical frameworks, low computing costs, and ease of implementation (e.g., Imamura et al. 1988; Kowalik and Bang, 1987; Liu et al. 1995; Titov and Synolakis, 1998). The hydrostatic governing equations describe wave propagation through the shallow-water celerity independent of the wave period. Recent advances in sensor technology have enabled detection of intricate dispersive wave systems even in large catastrophic tsunamis. Hanson and Bowman (2005) and Kulikov (2006) deduced separation of wave components by period in hydrophone and altimetry records of the 2004 Indian Ocean tsunami. Saito et al. (2010) and Yamazaki et al. (2011a) identified strong frequency dispersion in ocean-bottom pressure records of the 2010 Chile and 2011 Tohoku tsunamis. The observations show lagging of short-period components as the tsunami propagates across the ocean. Near the coast, Acoustic Doppler Current Profiler (ADCP) records have shown these trailing tsunami waves are the primary energy source for persistent surges and strong currents in tropical reef environments (Bricker et al., 2007; Yamazaki et al., 2012). Recognizing the importance, researchers have been exploring the use of numerical means in shallow-water models as well as high-order properties in Boussinesq-type or non-hydrostatic models to account for frequency dispersion during tsunami propagation.

Discretization of hyperbolic differential equations introduces truncation errors that can manifest as dispersion and dissipation in the numerical solution. The Taylor series expansion, which allows detailed analysis of discretization errors, is a classical approach

to evaluate these effects (Abbott et al., 1981; Warming and Hyett, 1974). Imamura et al. (1988) analyzed the staggered finite-difference scheme for the shallow-water equations and showed the grid size and time step can be adjusted to match the lead-order term of the dispersion relation from the Boussinesq-type equations of Peregrine (1967). Shuto (1991) and Burwell et al. (2007) demonstrated the use of numerical in place of physical dispersion through adjustment of the gird size in relation to the water depth for modeling of one-dimensional tsunami propagation. Cho (1995) extended the method to two dimensions by including corrections in the discretized shallow-water equations to mimic the cross-derivative dispersion terms in the Boussinesq-type equations for wave propagation oblique to a principal axis. Instead of adjusting the grid size locally, Cho et al. (2007) and Ha and Cho (2015) introduced variable coefficients in the correction terms to accommodate variation of water depth. Yoon (2002) proposed a variant of the approach by employing a *hidden* grid in the discretized equations with resolution tuned to account for dispersion at the local water depth. Wang and Liu (2011) adopted this approach to manipulate numerical dispersion for weakly nonlinear and weakly dispersive waves propagating over slowly-varying water depth with a shallow-water model.

More advanced, depth-integrated models can describe dispersion mathematically through the governing equations. One approach is to include high-order terms in the shallow-water equations through a Taylor series expansion of the dispersion relation from Airy wave theory (Peregrine, 1967). This gives rise to the Boussinesq-type equations of varying complexity commonly used in modeling of wind-generated waves (e.g., Gobbi et al., 2000; Madsen et al., 1991; Nwogu, 1993; Wei and Kirby, 1995;). Due to the high-order terms, Boussinesq-type models are typically implemented with a single computational grid to study transoceanic tsunami propagation (e.g., Horrillo et al., 2006; Kirby et al., 2013; Saito et al., 2014; Zhou et al., 2012). An alternate approach to describe

dispersive waves is to directly include the non-hydrostatic pressure and vertical velocity through the Keller-box scheme without increasing the order of the governing equations (Stelling and Zijlema, 2003). While a one-layer model is sufficient for tsunami modeling (Yamazaki et al., 2009), additional layers, instead of higher-order derivatives, are used to improve linear and nonlinear properties for modeling of wind-generated waves (e.g., Bai and Cheung, 2013; Smit et al., 2013; Zijlema et al., 2011). The relatively simple numerical framework allows implementation of a two-way grid-nesting scheme for modeling of tsunamis from trans-oceanic propagation to coastal runup (Yamazaki et al., 2011b). The vertical velocity also facilitates modeling of kinematic seafloor deformation to provide a more complete account of tsunami generation (e.g., Yamazaki et al., 2011a, 2018).

The governing equations of Boussinesq-type and non-hydrostatic models can account for dispersion to varying degree of accuracy in relation to the exact solution from Airy wave theory. While the dispersion relation of the Boussinesq-type equations converges asymptotically at the shallow-water limit, the low-order depth integration accompanying the Keller-box scheme leads to slight underestimation of dispersion in shoaling water for the non-hydrostatic approach (Bai et al., 2018). This is complicated by the discretization scheme, which modifies the governing equations and introduces truncation errors associated with the time step and grid size that interfere with the intrinsic dispersion property of the governing equations. Understanding of the numerical behaviors is crucial for selection of computational grids that can properly account for dispersion and make efficient use of computing resources. However, the truncation error analysis based on the Taylor series expansion becomes very cumbersome with the high-order derivatives in the Boussinesq-type equations. Vitousek and Fringer (2011) decoupled the intrinsic and numerical dispersion by assuming the water depth parameter is small and examined how

superposition of numerical dispersion from a shallow-water model to the intrinsic properties of the one-dimensional Boussinesq and KdV equations would modify internal wave propagation. As the intrinsic dispersion from the governing equations is highly accurate in shallow water, the discretization errors inevitably lead to underestimation of the celerity in the numerical solution.

In depth-integrated non-hydrostatic models, the discretization errors can potentially alleviate the underestimation of dispersion by the governing equations. The one-layer formulation, which provides the basic building block for multilayer models, serves as a proxy for examination of numerical dispersion in the non-hydrostatic approach. In this study, the non-hydrostatic system of governing equations is discretized with a staggered finite difference scheme in the two-dimensional horizontal plane and the Keller-box approach in the vertical direction. The non-hydrostatic terms involving the pressure and vertical velocity present a challenge in the truncation error analysis even though the governing equations remain at first order. The truncation error in the non-hydrostatic pressure is dependent on other variables effectively introducing high-order terms through recursive operations. Numerical dispersion is not directly additive to the intrinsic property of the non-hydrostatic system as demonstrated in the comparative model study of tsunami wave generation by Li et al. (2016). The Fourier method provides a straightforward procedure to derive the dispersion relation without directly involving the high-order and cross derivative terms as in the Taylor expansion approach.

Properly accounting for dispersion properties is not only essential for tsunami hazard mapping, but also for earthquake source investigation, in which tsunami Green's functions are computed and used in finite-fault inversion. The role of tsunami dispersion in source model inversion has received attention in recent years. Saito et al. (2010) and Hossen et al. (2015) demonstrated effects of dispersion on predicted tsunami source areas

4

using Green's functions generated by static initial pulses as finite sources on the sea surface, while Saito et al. (2011) estimated the initial sea-surface elevation for the 2011 Tohoku tsunami through inversion of the near-field DART and GPS records. Their Green's functions were generated by Boussinesq-type models. Romano et al. (2012, 2014) performed joint inversion of a finite-fault model using tsunami and geodetic records of the 2011 Tohoku event and accounting for dispersion during propagation through the non-hydrostatic NEOWAVE model of Yamazaki et al. (2009, 2011b). The use of vertical velocity, which describes dispersion in NEOWAVE, also enables to model kinematic seafloor deformation for a more complete resolving of tsunami generation. Yue et al. (2015) utilized this capability to compute Green's functions for joint inversion of the 2010 Mentawai *Mw* 7.8 earthquake. The resulting finite-fault model shows large, concentrated slip near the trench that is not evident in other studies. In light of numerical discretization, the use of a non-hydrostatic model does not necessarily ensure proper account of dispersion. A numerical dispersion relation can provide guidance for generation of Green's functions for inversion analyses.

This dissertation addresses the issue with numerical dispersion in non-hydrostatic modeling of long waves and investigates its implications for forward and inversion computations of tsunami waves. Chapter 2 describes the governing equations of the non-hydrostatic model using the Keller-box scheme, their linearization, and the discretization with the staggered finite-difference scheme. The Fourier expansion is used to derive the dispersion relation from the discretized governing equations that in turn is expanded by Taylor series for a lead-order approximation. Chapter 3 examines the effects of the discretization and depth parameters in the dispersion properties and explores the coupling between intrinsic and numerical dispersion. A series of numerical experiments using NEOWAVE examine the contribution of the implicit solution scheme to numerical

dispersion, highlight the anisotropic propagation properties over a two-dimensional computation grid, and demonstrate the use of numerical dispersion to offset errors intrinsic to the governing equations for better approximation of the exact solution from Airy wave theory. Chapter 4 presents a case study of the 2010 Mentawai earthquake and tsunami and investigates the effects of dispersion in the commonly-used source inversion techniques. NEOWAVE is used to perform hydrostatic and non-hydrostatic computations of tsunami Green's functions for the comparative study. Chapter 5 gives the conclusions of this research.

Chapter 2
Mathematical Formulation

The material in this chapter is part of the paper "Numerical dispersion in non-hydrostatic modeling of long-wave propagation" by Linyan Li and Kwok Fai Cheung that was submitted to Ocean Modelling in June 2018.

This chapter describes the two-dimensional depth-integrated governing equations for non-hydrostatic flows, their numerical discretization based on the staggered finite-difference scheme, and the derivation of numerical dispersion relation in terms of discretization and water depth parameters. Based on the linearized form of the governing equations with uniform water depth, the Fourier method is used to derive the dispersion relation through the solution to an eigen-value problem. The dispersion relation is then expanded by Taylor series to derive a lead-order approximation, which reveals the numerical and intrinsic dispersion properties and their interdependence more systematically.

2.1 Governing Equations

The free surface flow is defined by a Cartesian coordinate system (x, y, z) with the x and y axes in the horizontal plane and the positive z axis pointing upward in the vertical direction. Let g denote gravitational acceleration, h the water depth, and n the Manning roughness coefficient. Following the formulation from Yamazaki et al. (2009), the depth-integrated governing equations defines conservation of momentum in the x, y, and z directions as well as continuity of flow in the horizontal plane through

$$\frac{\partial U}{\partial t} + U\frac{\partial U}{\partial x} + V\frac{\partial U}{\partial y} = -g\frac{\partial \zeta}{\partial x} - \frac{\partial Q}{\partial x} - \frac{Q}{D}\frac{\partial(\zeta - h)}{\partial x} - n^2 \frac{g}{D^{1/3}}\frac{U\sqrt{U^2 + V^2}}{D} \qquad (1)$$

$$\frac{\partial V}{\partial t} + U\frac{\partial V}{\partial x} + V\frac{\partial V}{\partial y} = -g\frac{\partial \zeta}{\partial y} - \frac{\partial Q}{\partial y} - \frac{Q}{D}\frac{\partial(\zeta - h)}{\partial y} - n^2 \frac{g}{D^{1/3}}\frac{V\sqrt{U^2 + V^2}}{D} \qquad (2)$$

$$\frac{\partial W}{\partial t} + U\frac{\partial W}{\partial x} + V\frac{\partial W}{\partial y} = \frac{2Q}{D} \qquad (3)$$

$$\frac{\partial \zeta}{\partial t} + \frac{\partial(UD)}{\partial x} + \frac{\partial(VD)}{\partial y} = 0 \qquad (4)$$

where (U, V, W) is the depth-averaged velocity, ζ is the surface elevation, $D = \zeta + h$ is the flow depth, and Q denotes the depth-averaged non-hydrostatic pressure. The governing equations augment the shallow-water system with the non-hydrostatic pressure terms in the horizontal momentum equations (1) and (2) and the addition of the vertical momentum equation (3). The continuity equation (4) remains the same as in the shallow-water equations to ensure conservation of mass.

The Keller box scheme in Stelling and Zijlema (2003) defines the variables at the free surface and seabed. In deriving the horizontal momentum equations (1) and (2), the trapezoidal rule along with the dynamic free surface boundary condition of $q_\zeta = 0$ are invoked to approximate the depth-averaged non-hydrostatic pressure as

$$Q = \frac{1}{D}\int_{-h}^{\zeta} q \, dz \approx \frac{1}{2}(q_\zeta + q_b) = \frac{1}{2}q_b \qquad (5)$$

where q_b is the non-hydrostatic pressure at the bottom. The same rule integrates the vertical velocity w to give the depth-averaged W in the momentum equation (3) as

$$W = \frac{1}{D}\int_{-h}^{\zeta} w \, dz \approx \frac{1}{2}(w_\zeta + w_b) \qquad (6)$$

in which the vertical velocity at the free surface and bottom are given by the kinematic boundary conditions as

$$w_\zeta = \frac{\partial \zeta}{\partial t} + U\frac{\partial \zeta}{\partial x} + V\frac{\partial \zeta}{\partial y} \qquad z = \zeta \tag{7}$$

$$w_b = -U\frac{\partial h}{\partial x} - V\frac{\partial h}{\partial y} \qquad z = -h \tag{8}$$

For a linear variation of the vertical velocity over depth, the non-hydrostatic pressure should follow a quadratic distribution, but is also approximated as linear in the depth integration (5) following the Keller box scheme. This approximation leads to slight underestimation of dispersion in shoaling water with non-asymptotic convergence at the shallow-water limit even for a multi-layer model (Bai et al., 2018).

Dispersion analysis is based on linear wave propagation over constant water depth in the absence of bottom friction. The momentum equations and the continuity equation become

$$\frac{\partial U}{\partial t} = -g\frac{\partial \zeta}{\partial x} - \frac{\partial Q}{\partial x} \tag{9}$$

$$\frac{\partial V}{\partial t} = -g\frac{\partial \zeta}{\partial y} - \frac{\partial Q}{\partial y} \tag{10}$$

$$\frac{\partial W}{\partial t} = \frac{2Q}{h} \tag{11}$$

$$\frac{\partial \zeta}{\partial t} + h\frac{\partial U}{\partial x} + h\frac{\partial V}{\partial y} = 0 \tag{12}$$

The governing equations include terms of up to first order, but implicitly contain a third-order dispersion term as inferred from their equivalent Boussinesq form (Bai et al., 2018). There are four equations and five unknowns, U, V, W, ζ, and Q, in the non-hydrostatic system. Conservation of mass requires

$$\frac{\partial U}{\partial x} + \frac{\partial V}{\partial y} + \frac{\partial w}{\partial z} = 0 \tag{13}$$

in which

$$\frac{\partial w}{\partial z} = \frac{2W}{h} \tag{14}$$

for a linear profile of w over the water column. This fifth equation links the three velocity components and closes the system of equations for a solution.

The linearized governing equations (9) - (13) already include the discretization in the vertical direction through the depth integration (5) and (6) and the accompanying approximation of a linear profile in the Keller-box scheme. Figure 2.1 shows the staggered finite-difference grid for the discretization in the two-dimensional horizontal plane. The domain is divided into computational cells of dimensions Δx and Δy in the x and y directions. The horizontal velocity components U and V are defined at the cell interfaces ($i\pm 1/2, j$) and ($i, j\pm 1/2$), and the surface elevation ζ, vertical velocity W, and non-hydrostatic pressure Q at the cell center (i, j). The governing equations (9) to (13) are discretized as

$$\frac{U_{i+1/2,i}^{m+1} - U_{i+1/2,j}^{m}}{\Delta t} + g\frac{\zeta_{i+1,j}^{m} - \zeta_{i,j}^{m}}{\Delta x} + \frac{Q_{i+1,j}^{m+1} - Q_{i,j}^{m+1}}{\Delta x} = 0 \tag{15}$$

$$\frac{V_{i,j+1/2}^{m+1} - V_{i,j+1/2}^{m}}{\Delta t} + g\frac{\zeta_{i,j+1}^{m} - \zeta_{i,j}^{m}}{\Delta y} + \frac{Q_{i,j+1}^{m+1} - Q_{i,j}^{m+1}}{\Delta y} = 0 \tag{16}$$

$$\frac{W_{i,j}^{m+1} - W_{i,j}^{m}}{\Delta t} - \frac{2Q_{i,j}^{m+1}}{h} = 0 \tag{17}$$

$$\frac{\zeta_{i,j}^{m+1} - \zeta_{i,j}^{m}}{\Delta t} + h\frac{U_{i+1/2,j}^{m+1} - U_{i-1/2,j}^{m+1}}{\Delta x} + h\frac{V_{i,j+1/2}^{m+1} - V_{i,j-1/2}^{m+1}}{\Delta y} = 0 \tag{18}$$

$$\frac{U_{i+1/2,j}^{m+1} - U_{i-1/2,j}^{m+1}}{\Delta x} + \frac{V_{i,j+1/2}^{m+1} - V_{i,j-1/2}^{m+1}}{\Delta y} + \frac{2W_{i,j}^{m+1}}{h} = 0 \tag{19}$$

where the superscript m denotes the time step and Δt is the time step size. The time-integration scheme is first order, while the spatial derivatives are approximated by second-order central differences.
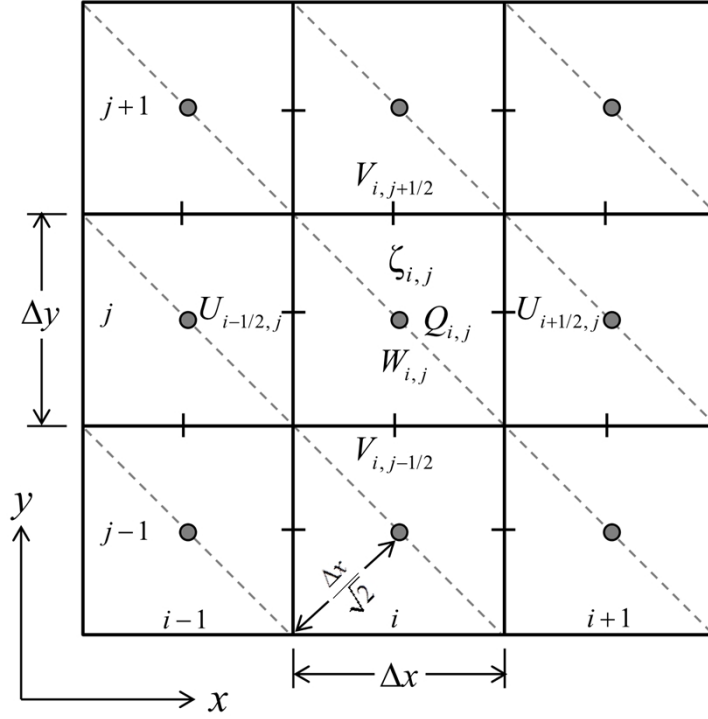
Figure 2.1 Schematic of staggered finite-difference scheme for the non-hydrostatic model and illustration of effective grid spacing for wave propagation at 45° from the *x* axis.

A semi-implicit approach evaluates the hydrostatic and non-hydrostatic components of the solution in two steps. The horizontal momentum equations (15) and (16), with non-hydrostatic pressure terms neglected, and the continuity equation (18) provide initial estimates for the horizontal velocity (U, V) and surface elevation ζ. Substitution of U, V and W, expressed in terms of the non-hydrostatic pressure Q from the momentum equations (15) - (17), into the mass conservation (19) gives the Poisson equation

$$
-\frac{\Delta t}{\Delta x^2}Q_{i-1,j}^{m+1} - \frac{\Delta t}{\Delta x^2}Q_{i+1,j}^{m+1} - \frac{\Delta t}{\Delta y^2}Q_{i,j-1}^{m+1} - \frac{\Delta t}{\Delta y^2}Q_{i,j+1}^{m+1} + \left(\frac{2\Delta t}{\Delta x^2} + \frac{2\Delta t}{\Delta y^2} + \frac{4\Delta t}{h^2}\right)Q_{i,j}^{m+1}
$$
$$
= -\frac{U_{i+1/2,j}^{*m+1} - U_{i-1/2,j}^{*m+1}}{\Delta x} - \frac{V_{i,j+1/2}^{*m+1} - V_{i,j-1/2}^{*m+1}}{\Delta y} - \frac{2W_{i,j}^m}{h}
$$

(20)

where the asterisk (*) denotes initial estimates from the hydrostatic step. The tri-diagonal matrix equation is solved implicitly for the non-hydrostatic pressure Q. The horizontal velocity (U, V) is then updated from integration of the non-hydrostatic terms in the momentum equations (15) and (16) and the vertical velocity W from equation (17). The surface elevation ζ is updated form the continuity equation (18) to complete the non-hydrostatic computation.

2.2 Fourier and Taylor Expansions

The discretization transforms the governing differential equations into a system of algebraic equations in which the grid size and time step function as free parameters modulating the numerical properties. In the Fourier expansion, each frequency component satisfies the governing equations and the resulting eigen-value matrix directly links the wave frequency and number in a dispersion relation with effects of the numerical discretization as phase errors. This analytical technique has been used to study numerical dispersion and stability in shallow-water models (e.g., Foreman, 1984; Leendertse, 1967; Sankaranarayanan and Spaulding, 2003). Its extension to the non-hydrostatic system simply involves two additional variables with the rank of the eigen-value matrix increased by two. The resulting dispersion relation expressed in trigonometric functions can in turn be expanded by Taylor series to illustrate systematically the order of the truncation errors as in the conventional approach.

We consider a system of regular progressive waves at uniform water depth. The variables ζ, U, V, W and Q are expressed as discrete Fourier modes over the staggered finite-difference grid in Figure 2.1 as

$$\zeta_{i,j}^m = \zeta_o e^{\mathrm{i}(ik_x\Delta x + jk_y\Delta y - m\omega\Delta t)} \tag{21}$$

$$U_{i+1/2,j}^{m} = U_o e^{i((i+1/2)k_x\Delta x + jk_y\Delta y - m\omega\Delta t)} \tag{22}$$

$$V_{i,j+1/2}^{m} = V_o e^{i(ik_x\Delta x + (j+1/2)k_y\Delta y - m\omega\Delta t)} \tag{23}$$

$$W_{i,j}^{m} = W_o e^{i(ik_x\Delta x + jk_y\Delta y - m\omega\Delta t)} \tag{24}$$

$$Q_{i,j}^{m} = Q_o e^{i(ik_x\Delta x + jk_y\Delta y - m\omega\Delta t)} \tag{25}$$

where ω is the wave frequency, k_x and k_y are the x and y components of the wave number vector $\vec{k}$ such that $k^2 = k_x{}^2 + k_x{}^2$, and the subscript o indicates the amplitude of the variables. Substitution of the discrete Fourier modes into the discretized governing equations (15) - (19) gives

$$\frac{U_o e^{i(k_x\Delta x/2)}(\lambda - 1)}{\Delta t} + g\frac{\zeta_o\left(e^{i(k_x\Delta x)} - 1\right)}{\Delta x} + \frac{Q_o\left(e^{i(k_x\Delta x)} - 1\right)\lambda}{\Delta x} = 0 \tag{26}$$

$$\frac{V_o e^{i(k_y\Delta y/2)}(\lambda - 1)}{\Delta t} + g\frac{\zeta_o\left(e^{i(k_y\Delta y)} - 1\right)}{\Delta y} + \frac{Q_o\left(e^{i(k_y\Delta y)} - 1\right)\lambda}{\Delta y} = 0 \tag{27}$$

$$\frac{W_o(\lambda - 1)}{\Delta t} - \frac{2Q_o\lambda}{h} = 0 \tag{28}$$

$$\frac{\zeta_o(\lambda - 1)}{\Delta t} + h\frac{U_o\left[2i\sin(k_x\Delta x/2)\right]\lambda}{\Delta x} + h\frac{V_o\left[2i\sin(k_y\Delta y/2)\right]\lambda}{\Delta y} = 0 \tag{29}$$

$$\frac{U_o\left[2i\sin(k_x\Delta x/2)\right]\lambda}{\Delta x} + \frac{V_o\left[2i\sin(k_y\Delta y/2)\right]\lambda}{\Delta y} + \frac{2W_o\lambda}{h} = 0 \tag{30}$$

where $\lambda = e^{-i\omega\Delta t}$ denotes the eigenvalue of the homogeneous system of equations. The system can be written in matrix form as

13

$$\begin{pmatrix} g\dfrac{2\mathrm{i}\sin\left(k_x\Delta x/2\right)}{\Delta x} & \dfrac{\lambda-1}{\Delta t} & 0 & 0 & \dfrac{\mathrm{i}\sin\left(k_x\Delta x/2\right)\lambda}{\Delta x} \\[2mm] g\dfrac{2\mathrm{i}\sin\left(k_y\Delta y/2\right)}{\Delta y} & 0 & \dfrac{\lambda-1}{\Delta t} & 0 & \dfrac{\mathrm{i}\sin\left(k_y\Delta y/2\right)\lambda}{\Delta y} \\[2mm] 0 & 0 & 0 & \dfrac{\lambda-1}{\Delta t} & -\dfrac{\lambda}{h} \\[2mm] \dfrac{\lambda-1}{\Delta t} & h\dfrac{2\mathrm{i}\sin\left(k_x\Delta x/2\right)\lambda}{\Delta x} & h\dfrac{2\mathrm{i}\sin\left(k_y\Delta y/2\right)\lambda}{\Delta y} & 0 & 0 \\[2mm] 0 & \dfrac{\mathrm{i}\sin\left(k_x\Delta x/2\right)\lambda}{\Delta x} & \dfrac{\mathrm{i}\sin\left(k_y\Delta y/2\right)\lambda}{\Delta y} & \dfrac{\lambda}{h} & 0 \end{pmatrix} \begin{pmatrix} \varsigma_o \\ U_o \\ V_o \\ W_o \\ Q_o \end{pmatrix} = 0 \quad (31)$$

While the wave number (k_x, k_y) is real, the angular frequency ω can be complex with real and imaginary parts representing dispersion and dissipation of the discretization scheme (Leendertse, 1967).

The matrix equation (31) represents propagation of a system of regular waves through the staggered finite-difference grid in Figure 2.1. A non-trivial solution requires the determinant of the matrix to be zero giving rise to

$$\frac{\lambda^2\left(1-\lambda\right)h^2}{\Delta t^3}\left\{\frac{h^2\left[1-\cos(k_x\Delta x)\right]}{2\Delta x^2}+\frac{h^2\left[1-\cos(k_y\Delta y)\right]}{2\Delta y^2}+1\right\}\left[\lambda^2+\left(2a-1\right)\lambda+1\right]=0 \quad (32)$$

in which

$$a=\frac{2gh\left[1-\cos\left(k_x\Delta x\right)\right]\Delta t^2\big/\Delta x^2+2gh\left[1-\cos\left(k_y\Delta y\right)\right]\Delta t^2\big/\Delta y^2}{2+h^2\left[1-\cos\left(k_x\Delta x\right)\right]\big/\Delta x^2+h^2\left[1-\cos\left(k_y\Delta y\right)\right]\big/\Delta y^2} \quad (33)$$

This can be satisfied by an eigenvalue of $\lambda=1$, which is equivalent to $\omega=0$ representing a steady flow. For wave propagation, the remaining eigenvalues take the form

$$\lambda=\left(1-a\right)\pm\mathrm{i}\sqrt{a(2-a)} \quad (34)$$

which has a modulus of one indicating $\mathrm{Im}(\omega)=0$ and the numerical scheme is non-dissipative. The eigenvalue $\lambda=e^{-\mathrm{i}\omega\Delta t}$ can alternatively be expressed as

14

$$\lambda = \cos(\omega\Delta t) - i\sin(\omega\Delta t) \qquad (35)$$

Comparison with equation (34) gives $\cos(\omega\Delta t) = (1-a)$ or

$$\cos(\omega\Delta t) = 1 - \frac{2gh\Delta t^2\Delta y^2\left[1-\cos(k_x\Delta x)\right] + 2gh\Delta t^2\Delta x^2\left[1-\cos(k_y\Delta y)\right]}{2\Delta x^2\Delta y^2 + h^2\Delta y^2\left[1-\cos(k_x\Delta x)\right] + h^2\Delta x^2\left[1-\cos(k_y\Delta y)\right]} \qquad (36)$$

which provides a dispersion relation for the discretized governing equations (26) to (30) in terms of the time step parameter $\omega\Delta t$ and the grid size parameters $k_x\Delta x$ and $k_y\Delta y$. Setting $\Delta x = \Delta y$ for square grid cells and introducing the Courant number $Cr = \sqrt{gh}\Delta t / \Delta x$, the dispersion relation can be expressed as

$$c = \sqrt{gh}\,\frac{1}{Cr(k\Delta x)}\arccos\left\{1 - \frac{2Cr^2(k\Delta x)^2\left[2-\cos\left(\sqrt{\alpha}k\Delta x\right)-\cos\left(\sqrt{1-\alpha}k\Delta x\right)\right]}{2(k\Delta x)^2 + (kh)^2\left[2-\cos\left(\sqrt{\alpha}k\Delta x\right)-\cos\left(\sqrt{1-\alpha}k\Delta x\right)\right]}\right\} \qquad (37)$$

where c is the celerity, kh is the water depth parameter, and $\alpha = k_x^2/k^2$ having a range of 0 to 1 for wave directions between 0 to 90° from the x axis. When $kh = 0$, equation (37) reduces to

$$c = \sqrt{gh}\,\frac{1}{Cr(k\Delta x)}\arccos\left\{1 - Cr^2\left[2-\cos\left(\sqrt{\alpha}k\Delta x\right)-\cos\left(\sqrt{1-\alpha}k\Delta x\right)\right]\right\} \qquad (38)$$

which is the dispersion relation of the hydrostatic model in terms of the spatial and temporal discretization parameters.

The dispersion relation (37) is the exact solution to the discretized governing equations (15) to (19), but does not fully reveal the interplay between the depth and discretization parameters. To illustrate the lead-order structure, we expand the cosine functions in equation (36) about $k_x\Delta x = 0$, $k_y\Delta y = k_y\Delta x = 0$, and $\omega\Delta t = 0$ by Taylor series to give

$$\frac{1}{\Delta t^2}\left[\frac{(\omega\Delta t)^2}{2}-\frac{(\omega\Delta t)^4}{24}\right]=\frac{gh\left[\left(k_x^{\,2}+k_y^{\,2}\right)\Delta x^2-\dfrac{\left(k_x^{\,4}+k_y^{\,4}\right)\Delta x^4}{12}\right]}{2\Delta x^2+h^2\left[\dfrac{\left(k_x^{\,2}+k_y^{\,2}\right)\Delta x^2}{2}-\dfrac{\left(k_x^{\,4}+k_y^{\,4}\right)\Delta x^4}{24}\right]}+\mathrm{O}\left(\Delta x^4,\Delta t^4\right) \quad (39)$$

Substitution of $\omega=ck$ into equation (39) gives

$$c^2-\frac{c^4}{12}(k\Delta t)^2=gh\frac{1-\dfrac{1}{12}(k\Delta x)^2+\dfrac{k_x^{\,2}k_y^{\,2}}{6k^2}\Delta x^2}{1+\dfrac{1}{4}(kh)^2\left[1-\dfrac{1}{12}(k\Delta x)^2+\dfrac{k_x^{\,2}k_y^{\,2}}{6k^2}\Delta x^2\right]}+\mathrm{O}\left(\Delta x^4,\Delta t^4\right) \quad (40)$$

where truncation errors of fourth order or higher are grouped under O(Δx^4, Δt^4). The relation can be rewritten with the c^4 term as truncation errors as

$$c^2=gh\frac{1-\dfrac{1}{12}(k\Delta x)^2+\dfrac{k_x^{\,2}k_y^{\,2}}{6k^2}\Delta x^2}{1+\dfrac{1}{4}(kh)^2\left[1-\dfrac{1}{12}(k\Delta x)^2+\dfrac{k_x^{\,2}k_y^{\,2}}{6k^2}\Delta x^2\right]}+\mathrm{O}\left(\Delta x^4,\Delta t^2\right) \quad (41)$$

Substituting equation (41) into the c^4 term in equation (40) gives

$$c^2=gh\frac{1-\dfrac{1}{12}(k\Delta x)^2+\dfrac{k_x^{\,2}k_y^{\,2}}{6k^2}\Delta x^2}{1+\dfrac{1}{4}(kh)^2\left[1-\dfrac{1}{12}(k\Delta x)^2+\dfrac{k_x^{\,2}k_y^{\,2}}{6k^2}\Delta x^2\right]}$$

$$+\frac{1}{12}(gh)^2\frac{\left[1-\dfrac{1}{12}(k\Delta x)^2+\dfrac{k_x^{\,2}k_y^{\,2}}{6k^2}\Delta x^2\right]^2(k\Delta t)^2}{\left\{1+\dfrac{1}{4}(kh)^2\left[1-\dfrac{1}{12}(k\Delta x)^2+\dfrac{k_x^{\,2}k_y^{\,2}}{6k^2}\Delta x^2\right]\right\}^2}+\mathrm{O}\left(\Delta x^4,\Delta t^4\right) \quad (42)$$

By neglecting fourth and higher-order terms in $k\Delta x$ and $\omega\Delta t$, we have the lead-order non-hydrostatic dispersion relation

$$c = \sqrt{gh} \left\{ \frac{1}{1 + \frac{1}{4}(kh)^2} - \frac{\frac{1}{12}(k\Delta x)^2 (\beta - Cr^2)}{\left[1 + \frac{1}{4}(kh)^2\right]\left[1 + \frac{1}{4}(kh)^2 - \frac{\beta}{24}(kh)^2 (k\Delta x)^2\right]} \right\}^{1/2}$$ (43)

where $\beta = 1 - 2k_x^2 k_y^2 / k^4$ varying between 1 and 0.5 for wave propagating along the principal axes and the diagonal at 45°. Introducing $\Delta x^2 = \gamma h^2 + gh\Delta t^2$, which is a generalization from Imamura et al. (1988), gives

$$c = \sqrt{gh} \left\{ \frac{1 + \left[\frac{1}{4} - \frac{\gamma(\beta - Cr^2)}{12(1 - Cr^2)}\right](kh)^2 - \frac{\gamma\beta}{24(1 - Cr^2)}(kh)^4}{1 + \frac{1}{2}(kh)^2 + \left[\frac{1}{16} - \frac{\gamma\beta}{24(1 - Cr^2)}\right](kh)^4 - \frac{\gamma\beta}{96(1 - Cr^2)}(kh)^6} \right\}^{1/2}$$ (44)

where $\gamma = (\Delta x^2 - gh\Delta t^2)/h^2$ is a parameter that combines grid size, time step, and water depth. In the absence of discretization errors, the numerical dispersion term vanishes and both equations (43) and (44) reduce to

$$c = \sqrt{gh} \left[1 + \frac{1}{4}(kh)^2\right]^{-1/2}$$ (45)

which is the intrinsic dispersion relation of the governing equations (9) - (13) for the non-hydrostatic system. A comparison between equations (44) and (45) illustrates that the discretization augments the order of the dispersion relation from a [0, 2] to a [4, 6] rational function expansion along with introduction of the tuning parameter γ for optimization.

The lead-order dispersion relation (43) is consistent with a Taylor series expansion of the truncation errors in the discretized governing equations (15) to (19) of the non-hydrostatic system and is strictly valid for small values of the discretization for

17

illustration. When $kh = 0$, the non-hydrostatic terms in the governing equations vanish and the dispersion relation reduces to

$$c = \sqrt{gh}\left[1-\frac{\beta}{12}(k\Delta x)^2 + \frac{1}{12}Cr^2(k\Delta x)^2\right]^{1/2} \qquad (46)$$

A $\beta = 1$ results in the dispersion relation derived by Imamura et al. (1988) for wave propagation along a principal axis. Substitution of $\Delta x^2 = \gamma h^2 + gh\Delta t^2$ yields

$$c = \sqrt{gh}\left[1-\frac{\gamma}{12}(kh)^2\right]^{1/2} \qquad (47)$$

where kh is introduced into the hydrostatic dispersion relation to account for depth-dependence of discretization errors. Imamura et al. (1988) showed a value of $\gamma = 4$ gives rise to

$$c = \sqrt{gh}\left[1-\frac{1}{3}(kh)^2\right]^{1/2} \qquad (48)$$

which is the lead-order expansion of the dispersion relation from the Boussinesq-type equations of Peregrine (1967). The coefficient 1/3 corresponds to the dispersion term of the governing equations and yields good approximation in shallow water with asymptotic convergence to Airy wave theory at $kh = 0$. In comparison, the dispersion term in the Boussinesq form of the non-hydrostatic system has a coefficient of 1/4 (Bai and Cheung, 2013), which leads to slight underestimation of the dispersion in shoaling water as depicted by equation (45).

Chapter 3
Wave Dispersion

The material in this chapter is part of the paper "Numerical dispersion in non-hydrostatic modeling of long-wave propagation" by Linyan Li and Kwok Fai Cheung that was submitted to Ocean Modelling in June 2018.

The dispersion relation derived in Chapter 2 enable examination of the propagation characteristics in terms of the discretization and depth parameters for both hydrostatic and non-hydrostatic models. In this chapter, these effects are investigated through the celerity from the dispersion relation as a function of water depth, gird size, time step and wave direction with the aid of the lead-order approximation as well as one-dimensional and two-dimensional numerical experiments performed by NEOWAVE. The one-dimensional numerical experiment involves standing waves of a given wavelength and provides the corresponding wave period for computation of the celerity. Comparison of the computed celerity with the dispersion relation shows the influence of computational error from the implicit scheme of the non-hydrostatic pressure term. The two-dimensional tests use a Gaussian hump as initial conditions with wavelength, water depth, and spatial grid size relevant to tsunami modeling and demonstrate the interplay between intrinsic and numerical dispersion. The numerical dispersion properties along oblique directions to the grid axis are also explored. These also include examination of the use of discretization errors to mimic or enhance dispersion in matching Airy wave theory for wave modeling in tsunami range.

3.1 Dispersion Relations

Both dispersion relations (37) and (43) give the celerity in terms of the water depth parameter kh, discretization parameters $k\Delta x$ and Cr, and the relative wave direction; the latter, lead-order form shows systematically the role of each parameter and its inter-relationship with the others. The lead-order approximation clearly delineates the intrinsic and numerical dispersion in two separate terms. The celerity decreases with kh due to intrinsic dispersion from the governing equations, but the spatial discretization also influence the results through numerical dispersion. While the theoretical upper bound of $k\Delta x$ is π equivalent to the Nyquist frequency, the practical maximum for wave modeling is around one, corresponding to six computational cells per wavelength, such that the denominator of the dispersion term in the lead-order approximation (43) is positive. The parameter $k\Delta x$, which is also in the numerator, always reduces the celerity through numerical dispersion. The complementary effects of kh and $k\Delta x$ provides the basis for the use of spatial discretization errors to optimize dispersion properties in hydrostatic wave models. The two parameters, however, are coupled in modulating numerical dispersion in the non-hydrostatic model. The presence of kh in the denominator of the second term indicates reduction of numerical dispersion with water depth. The Courant number Cr must be less than one and preferable below 0.5 for a semi-implicit scheme. Since the denominator is always positive in practical application, the temporal discretization tends to increase the celerity while reducing numerical dispersion.

The lead-order dispersion relation (43) is valid for small values of the discretization parameters. To aid interpretation, Figure 3.1a plots the celerity from the exact relation (37) over $k\Delta x$ and Cr with the propagation direction along the x axis. The considered range of depth parameters $0 \leq kh \leq 0.6$ is most relevant to tsunami modeling. The celerity decreases and dispersion increases with kh and $k\Delta x$, but vice versa with Cr. The Courant

number plays a secondary role in counteracting numerical dispersion because of its coupling with $k\Delta x$ resulting in a combined fourth order term as shown in the lead-order approximation. Oblique wave propagation also reduces numerical dispersion. Figure 3.1b demonstrates the increased celerity with an oblique wave direction of 45° from the x axis. The lead-order dispersion relation (43) can provide some insights into the mechanism. The parameter β can be absorbed into the discretization parameter as $k(\sqrt{\beta}\Delta x)$ to denote an effective grid spacing in terms of the wave direction relative to the x axis. Since $\beta \leq 1$, the effective decrease in grid size reduces numerical dispersion for oblique wave propagation. Turning the waves to 45° with $\beta = 1/2$ has the same effects on the celerity as a reduction of the grid size by a factor of $1/\sqrt{2}$ as illustrated geometrically in Figure 2.1. The results also show increased influence of Cr at the smaller value of $\beta = 1/2$ as indicated in the lead-order dispersion relation (43).
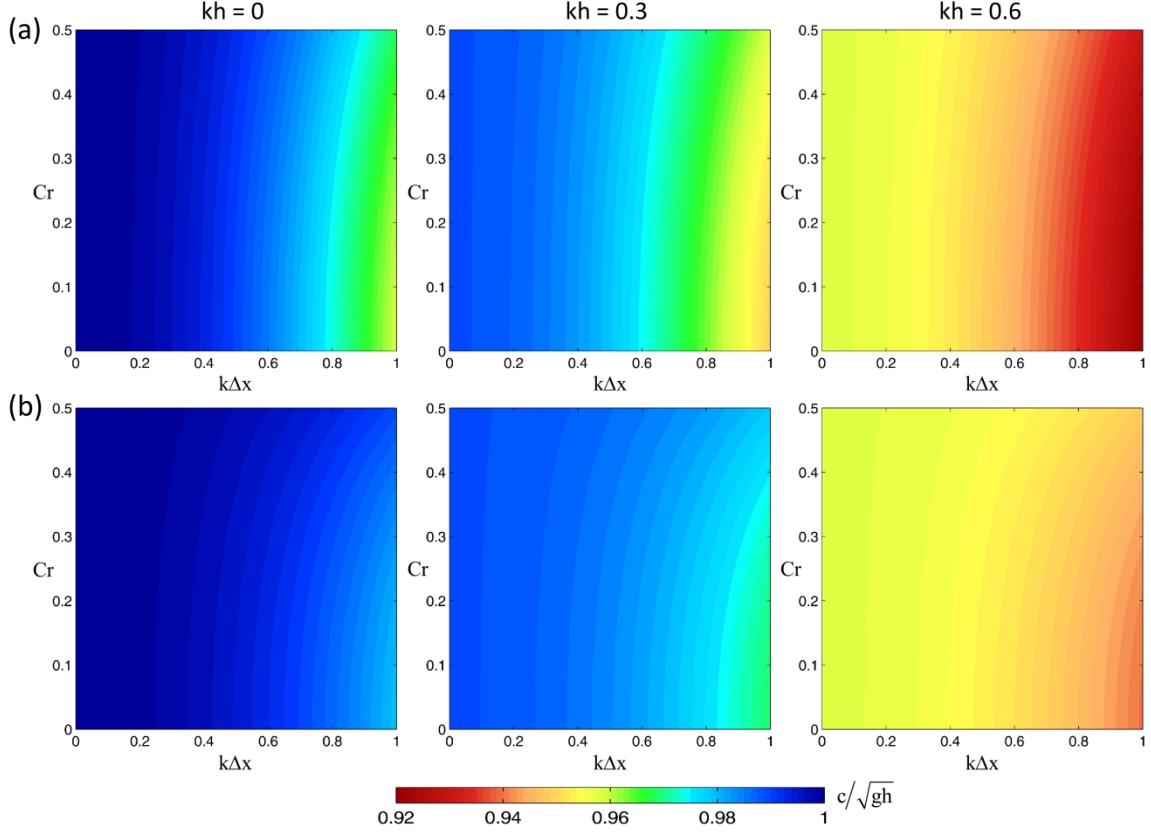
Figure 3.1 Celerity normalized by shallow-water theory as a function of $k\Delta x$ and Cr. (a) Wave propagation along the x axis. (b) Propagation at 45° from the x axis.

The dispersion relation (37) also provides a tool to elucidate the interplay between numerical and intrinsic dispersion in matching Airy wave theory. We consider waves propagating along the x axis to illustrate tuning of the dispersion relation for specific applications. The concept of effective grid size can be applied to infer the dispersion property for oblique wave directions. Figure 3.2 plots the computed celerity normalized by the exact solution from Airy wave theory over $k\Delta x$ and Cr. The intrinsic dispersion relation, which emerges at $k\Delta x = 0$, overestimates the celerity in both the hydrostatic and non-hydrostatic solution when $kh > 0$. Numerical dispersion can make up for the deficiency in matching the exact solution through a combination of spatial and temporal discretization errors. The hydrostatic model, however, requires a grid size of $k\Delta x > 0.6$ to

achieve the correct dispersion property outside the shallow-water range. A slightly larger grid size is needed to counter the effects of temporal discretization. Inclusion of the non-hydrostatic terms in the governing equations alleviates this requirement and enables achievement of proper dispersion within the range of $k\Delta x$ suitable for tsunami modeling.
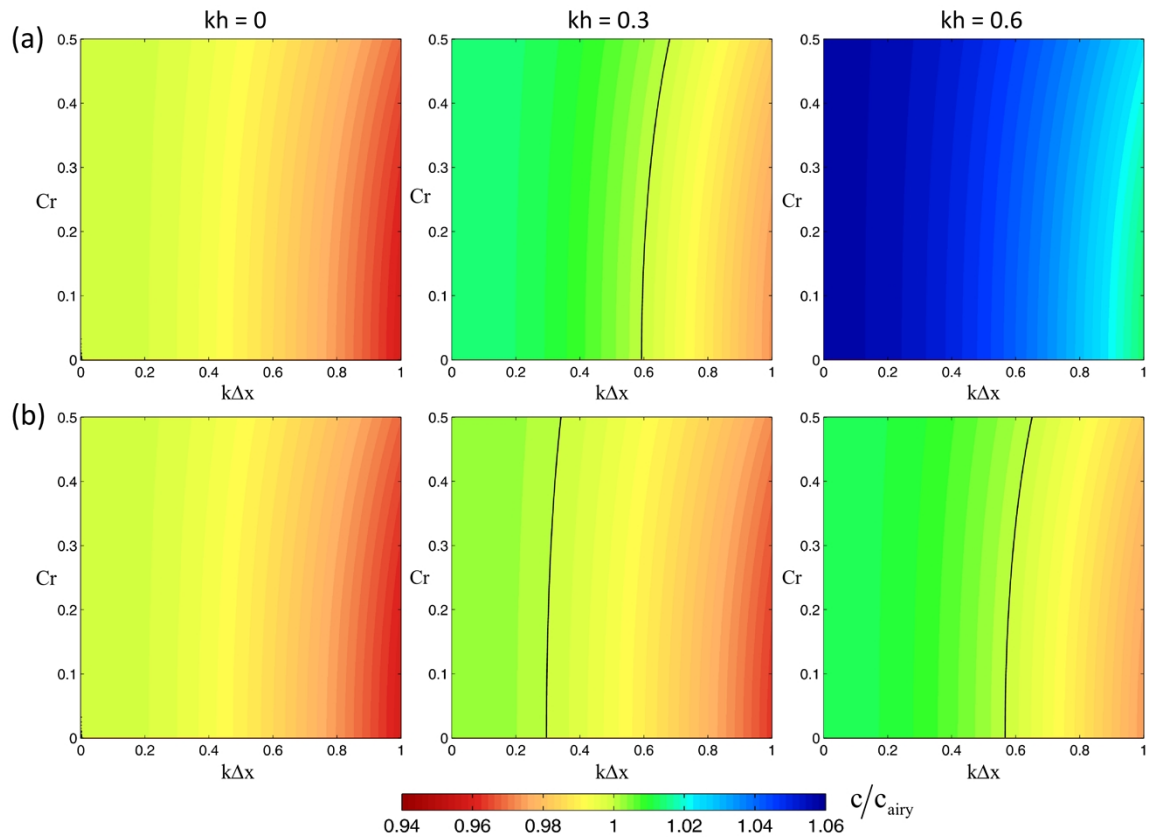
Figure 3.2 Celerity normalized by Airy wave theory as a function of $k\Delta x$ and Cr. (a) Hydrostatic model. (b) Non-hydrostatic model.

A tsunami consists of a wide range of harmonics associated with the complexity of the seafloor deformation from earthquake rupture. Since the harmonic components are defined in terms of the wavelength at the source, dispersion is key to reproduction of the wave period distribution. It is therefore important to match the dispersion relation from Airy wave theory over a wide range of water depth parameters. Figure 3.3a plots the

normalized celerity from the hydrostatic dispersion relation (38) as a function of kh introduced by substitution of $\Delta x^2 = \gamma h^2 + gh\Delta t^2$. Since the time step size plays a secondary role in numerical dispersion, we assign $Cr = 0.01$ to focus on the effects of spatial discretization. With $\Delta t \rightarrow 0$, the combined grid size and depth parameter $\gamma = (\Delta x/h)^2$ effectively relates the numerical component of the model celerity versus the intrinsic component from the governing equations. The results illustrate strong dependence of numerical dispersion on the water depth parameter. A value of $\gamma = 4$, which reproduces the lead-order term of the dispersion relation from the Boussinesq-type equations of Peregrine (1967), provides a very good approximation of the celerity from Airy wave theory around shallow water. The resulting dispersion relation has a 0.53% error at $kh = 0.6$ for reference. However, the large grid size at two times the water depth leads to excessive numerical dispersion at large values of kh. Decreasing the value of γ leads to lower numerical dispersion and larger celerity approaching the shallow-water solution indicated as $\gamma = 0$. The lack of dispersion results in substantial overestimation of the celerity with increasing kh.

The discretization errors can similarly be tuned to augment the non-hydrostatic dispersion relation (37) for improved wave propagation characteristics as shown in Figure 3.3b. A large value of $\gamma = 4$ results in excessive numerical dispersion leading to underestimation of the celerity even within the shallow-water range. Reducing γ leads to increase of the celerity, but at a lower rate over a smaller range comparing to the hydrostatic model results in Figure 3.3a. The non-hydrostatic terms in the governing equations reduce the effects of spatial discretization, as already indicated in the lead-order dispersion relation (43), thereby improving numerical modeling of wave propagation over varying depth or across nested computational grids. In comparison to Airy wave theory, the intrinsic dispersion relation (45) denoted by $\gamma = 0$ slightly

underestimates dispersion for $kh < 2.4$. A value of $\gamma = 0.8$ introduces the right amount of numerical dispersion to offset the underestimation in reproducing the celerity up to $kh = 0.6$ and 1 with less than 0.13% and 0.24% error comparing to Airy wave theory. The resulting dispersion relation follows closely the Boussineq-type equations of Peregrine (1967) for tsunami modeling and has slightly better performance over most of the intermediate depth range. The non-hydrostatic model can similarly be tuned to a wider range of kh for computation of surf-zone processes involving wind-generated waves. The use of the Boussinesq-type equations, which can provide accurate description of dispersion in theory, inevitably results in unwarranted dispersion in the numerical solution.
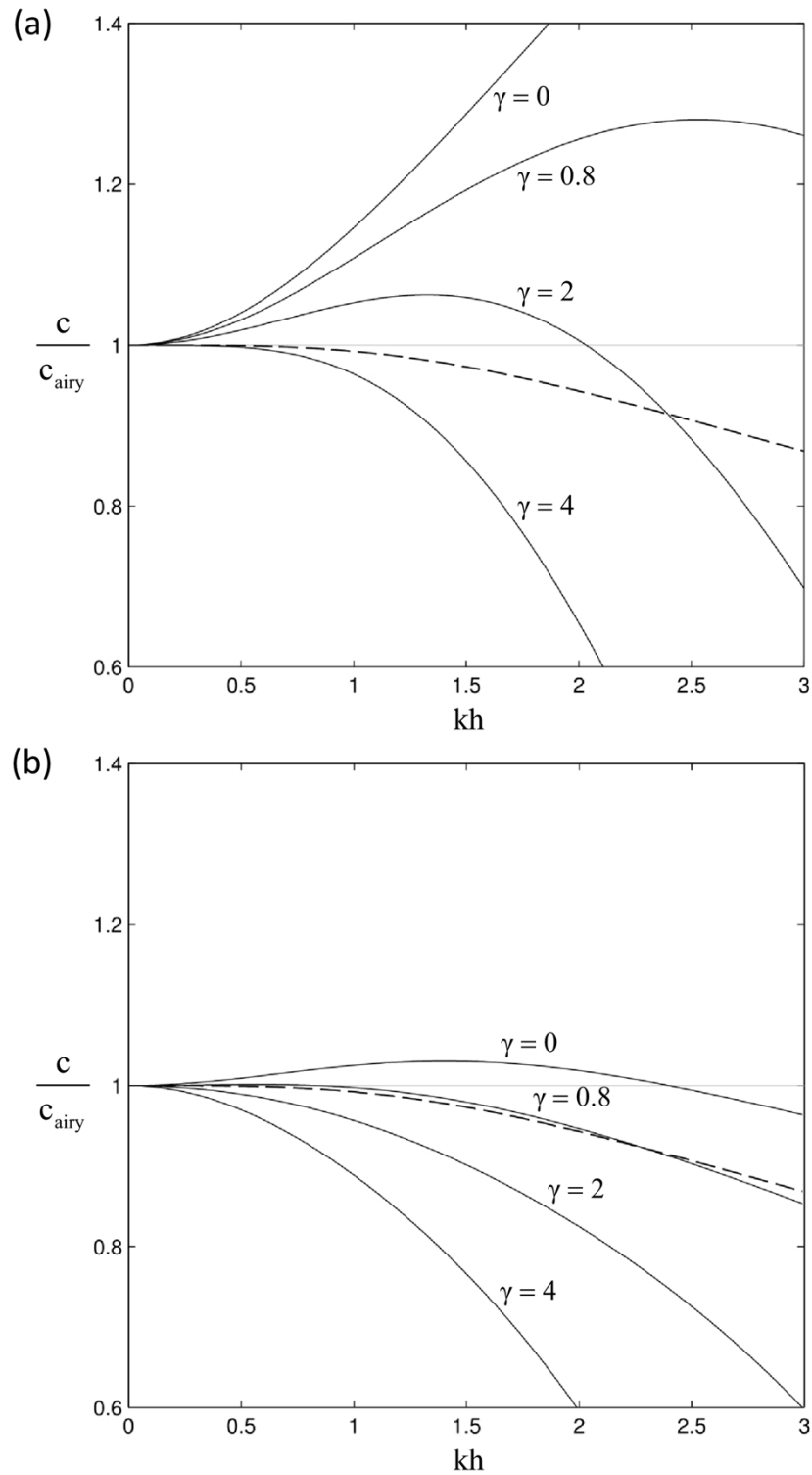
Figure 3.3 Celerity normalized by Airy wave theory as a function of *kh*. (a) Hydrostatic model. (b) Non-hydrostatic model. Solid and dash lines indicate celerity from the dispersion relation (37) and the Boussinesq-type equations of Peregrine (1967).

3.2 Numerical Examples

The non-hydrostatic dispersion relation (37) is independent of the semi-implicit solution involving the pressure Poisson equation (20). The effects of the solution scheme and its computational errors on dispersion are first examined through a one-dimensional numerical experiment using the non-hydrostatic NEOWAVE model, which is based on the staggered finite-difference and Keller-box schemes described in Chapter 2. Dispersion in a numerical model can be evaluated from standing waves of a given wavelength (Bai and Cheung, 2016). Figure 3.4 shows a schematic to illustrate the standing wave experiment. The initial static condition corresponds to a sinusoidal wave profile with a very small amplitude compared to the wavelength and water depth to minimize nonlinear effects. Zero elevation is imposed at the open boundaries to restrain the node locations and subsequently the length of the standing waves. A numerical gauge at the center of the flume records the surface elevation time series, which allows estimation of the period for computation of the celerity for the given wavelength.
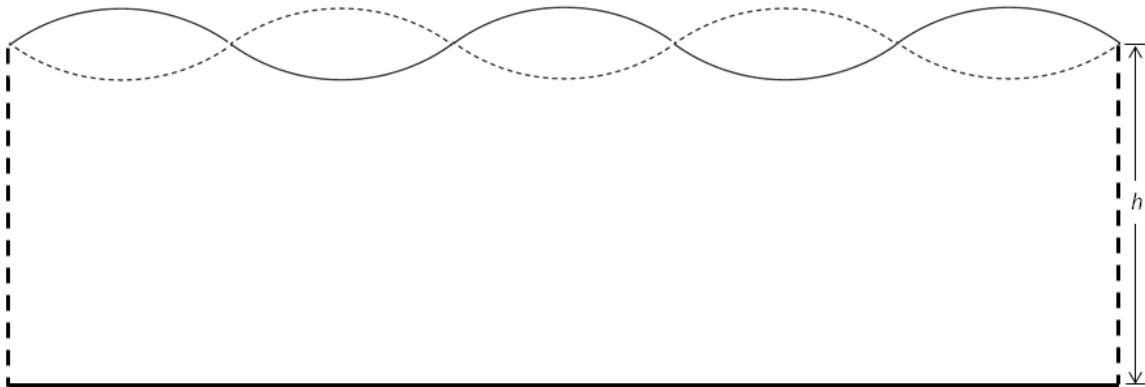
Figure 3.4 Schematic of numerical experiments for standing waves.

Adjustment of the water depth, time step, and grid size allows comparison of the numerical model results with the non-hydrostatic dispersion relation (37) in terms of the

non-dimensional parameters kh, $k\Delta x$, and Cr. Figure 3.5a shows the celerity as a function of $k\Delta x$ for kh up to 0.6 and a small $Cr = 0.1$. The numerical model and the dispersion relation (37) give almost identical results at $kh = 0$, which correspond to the hydrostatic conditions and provide a baseline for comparison. The discrepancies increase slightly with $k\Delta x$ for $kh > 0$, when the semi-implicit scheme is involved in the numerical solution. The computational errors, however, are very small comparing to the discretization errors in governing dispersion properties in the numerical model. Also included in the comparison is the lead-order approximation (43), which is almost identical to the dispersion relation (37) for $k\Delta x < 0.6$ independent of kh, which is not used in the Taylor series expansion. As the accuracy is to second order, minor discrepancies develop at large values of $k\Delta x$ that are outside the range for numerical modeling. Figure 3.5b shows the celerity as a function of Cr while minimizing the spatial discretization errors by setting $k\Delta x = 0.1$. Because of the small values of $k\Delta x$, the celerity is not very sensitive to Cr (See Figure 3.1a). The good agreement between the model and analytical results over the full range of Cr reconfirms that the time step plays a secondary role in numerical dispersion.
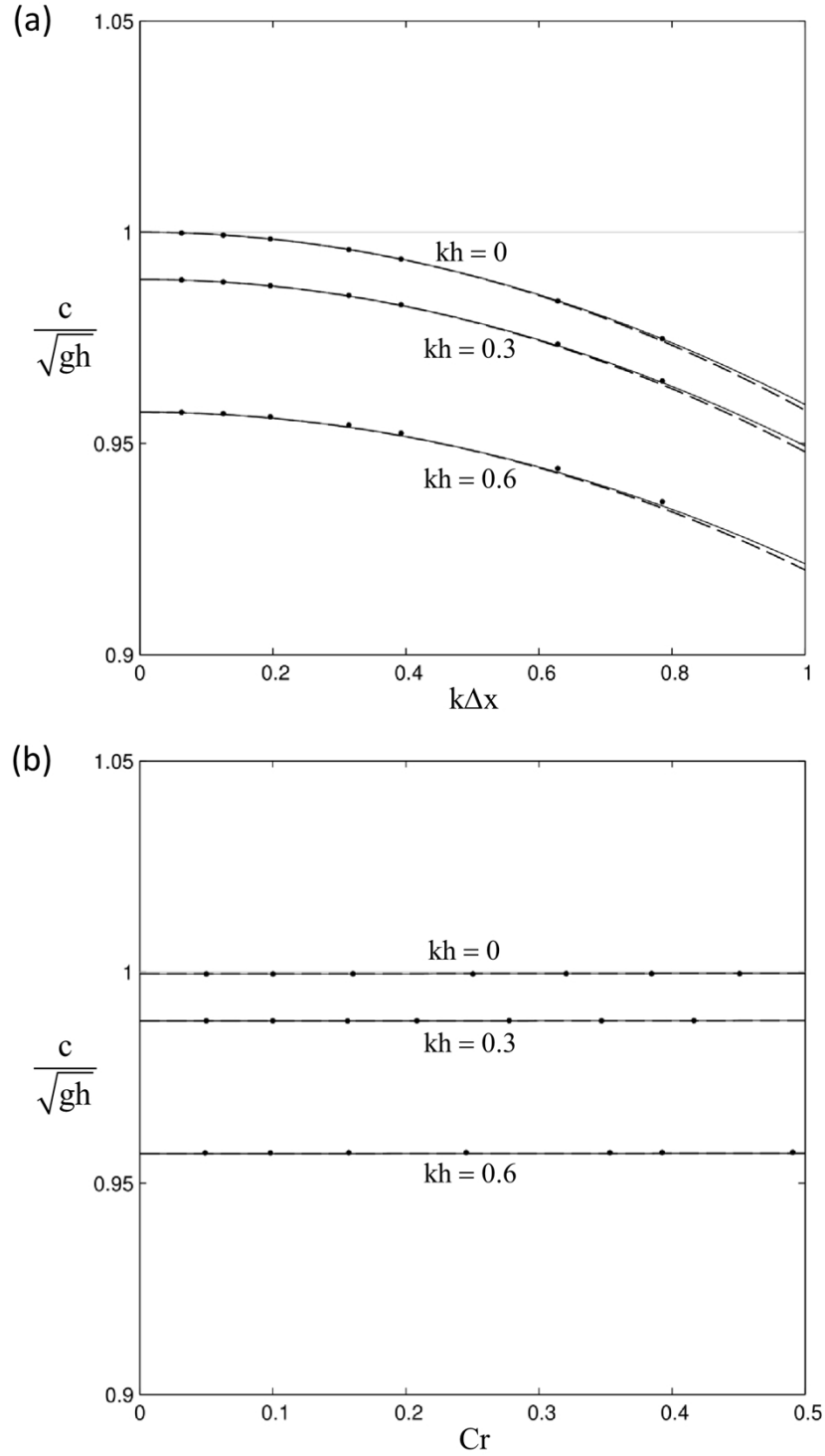
Figure 3.5 Celerity normalized by shallow-water theory as a function of discretization parameters. (a) Grid size parameter $k\Delta x$. (b) Courant number Cr. Solid lines, dash lines, and dots denote celerity from the dispersion relation (37), the lead-order approximation (43), and numerical experiments.

We utilize a second set of numerical experiments to illustrate manifestation of spatial discretization errors in wave propagation and anisotropy of wave dispersion over a two-dimensional computational grid. The numerical experiments involve a square domain with initial conditions defined by a Gaussian hump at the center

$$\zeta(r) = e^{-r^2/(b/4)^2} \tag{47}$$

where r is radial distance and b is effectively the diameter at the still-water level. The hump, which contains a range of spatial harmonics, is analogous to the initial conditions commonly used for tsunami modeling. The waves propagate radially from the center with celerity and period determined from the dispersion relation. Although the physical problem is axisymmetric, the numerical solution depends on the wave direction relative to the principal axis of the computational grid. The effects of the Courant number is independent of the wave direction. We utilize a small $Cr = 0.01$ to focus on the spatial discretization, which dominates numerical dispersion. The domain has a uniform water depth of 4 km representing the average of the Pacific Ocean. The selected grid sizes of 3.6, 5.7, and 8 km correspond to $\gamma = 0.8$, 2, and 4 for small Courant numbers. The 3.6-km grid is close to 2 arcmin near the equator and is commonly used to model trans-Pacific tsunami propagation. The corresponding value of $\gamma = 0.8$ also gives the best dispersion properties in the non-hydrostatic model comparing to Airy wave theory as shown in Figure 3.3b. The grid size of 5.7 km is approximately 3 arcmin, representing an intermediate value that has been used in tsunami modeling. The grid size of 8 km or 4.5 arcmin, which might not fully resolve the seamounts and atolls in the Pacific, is included here to demonstrate the convergence of the hydrostatic dispersion relation at $\gamma = 4$ to Airy wave theory in shallow water.

The first series of tests utilize an effective diameter of $b = 120$ km for the Gaussian hump that the dominant harmonic is well within the shallow water range. Figure 3.6a

plots the time series and spectra at 1500 km from the center along the x axis. The non-hydrostatic solution with $\gamma = 0.8$, which closely follows the dispersion relation from Airy wave theory up to $kh = 1$, provides a baseline for comparison. The waveform shows a distinct crest and trough profile in the form of an N-wave followed by dispersive waves with decreasing amplitude and period associated with the higher harmonics in the initial conditions. The spectrum has a peak period of 12.2 min or $kh = 0.17$ and a shortest period of 3 min or $kh = 0.77$. The hydrostatic solution shows a typical crest and trough profile with a larger amplitude and peak period due to low numerical dispersion in the shallow-water range. Since the numerical scheme is not dissipative, the energy should be conserved in the system. The energy of the surface signals is less probably due to the higher velocity and celerity in the less dispersive flow. The non-hydrostatic solution still provides a reasonable description for the main wave component at $\gamma = 2$ albeit with a slight increase in the amplitude and period of the dispersive waves. The hydrostatic solution shows development of trailing waves with increased numerical dispersion. At $\gamma = 4$, the non-hydrostatic solution overestimates dispersion with notable transfer of energy from the leading to the trailing waves. The hydrostatic solution closely matches the dispersion relation of Airy wave theory up to $kh = 0.6$ and produces very similar results as the non-hydrostatic solution with $\gamma = 0.8$ as shown in Figure 3.6b. The similar amplitude spectra and energy levels in the two cases, albeit with distinct grid resolutions, is due entirely to the close approximation of the celerity.

Figure 3.6 Time series and spectra at 1500 km along the *x* axis resulting from a Gaussian hump with an effective diameter of 120 km at the center. (a) Effects of the combined grid size and depth parameter γ. (b) Comparison of the hydrostatic and non-hydrostatic solutions with γ = 4 and 0.8 respectively. Black and red lines denote hydrostatic and non-hydrostatic solutions.

The second series of tests utilize an effective diameter of $b = 60$ km for the Gaussian hump that is representative of the detailed seafloor rupture in the 2011 Tohoku earthquake (Yamazaki et al., 2018). Figure 3.7a plots the time series and spectra at 1500 km from the center along the x axis. For the non-hydrostatic solution with $\gamma = 0.8$, the time series shows a wave train with decreasing amplitude and period typical of a dispersive system. The spectrum has a peak period of 5 min or $kh = 0.44$ and the shortest period of 2.5 min or $kh = 0.96$ within the accurate range of dispersion to set a baseline. The corresponding hydrostatic solution produces a distinct initial peak and trough profile followed by short-period waves down to 1.5 min. Since the initial conditions defines the spectral components in terms of the wavelength, the overestimated celerity, as shown in Figure 3.3a, leads to underestimation of the wave periods. Dispersion is instrumental in eliminating these non-physical short-period trailing waves commonly seen in hydrostatic model results. The non-hydrostatic solution still provides reasonable results for the main wave component at $\gamma = 2$, but the slightly underestimated celerity results in overestimation of the period and amplitude for the shorter waves. With increased numerical dispersion, the hydrostatic solution shows longer trailing waves and improved description of wave attenuation. At $\gamma = 4$, the non-hydrostatic solution overestimates the amplitude and period of the trailing waves due to the large grid size. The hydrostatic solution reproduces the dispersion in the shallow-water range and the longer-period initial waves from the non-hydrostatic solution with $\gamma = 0.8$ as shown in Figure 3.7b. The excessive numerical dispersion in intermediate depth results in persistent, short-period trailing waves and overestimation of the spectral energy of the surface signals.
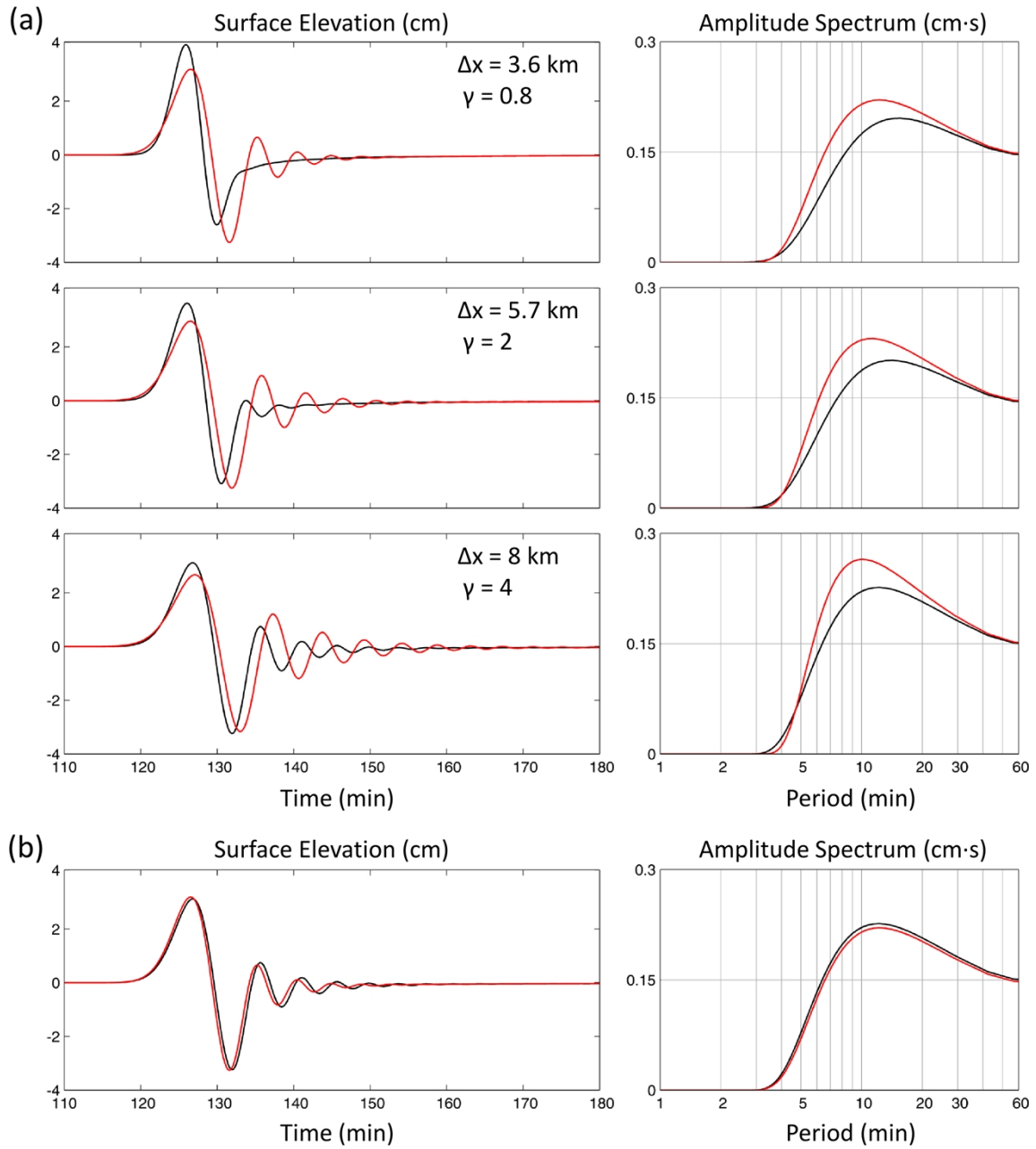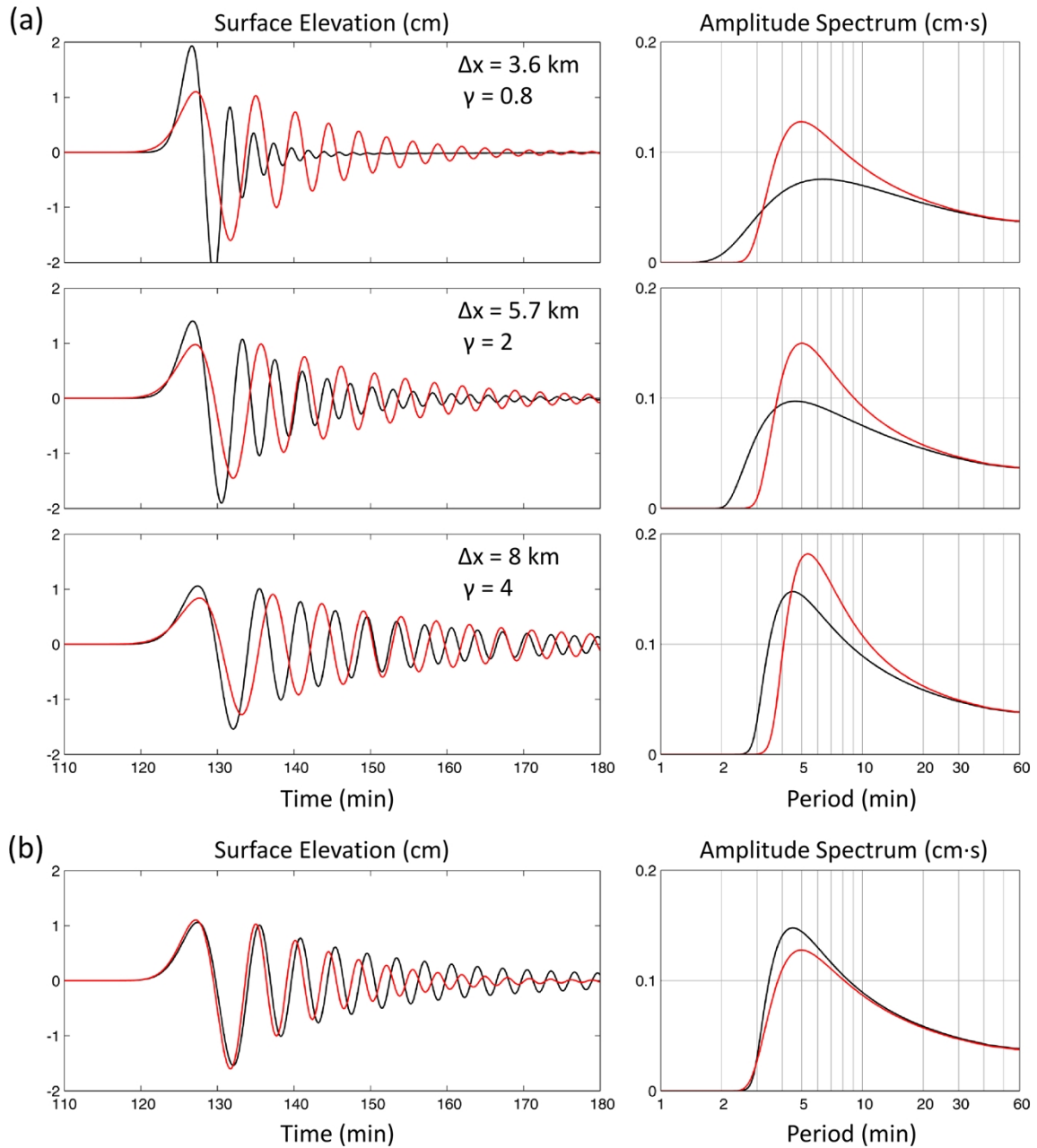
Figure 3.7 Time series and spectra at 1500 km along the *x* axis resulting from a Gaussian hump with an effective diameter of 60 km at the center. (a) Effects of the combined grid size and depth parameter γ. (b) Comparison of the hydrostatic and non-hydrostatic solutions with γ = 4 and 0.8 respectively. Black and red lines denote hydrostatic and non-hydrostatic solutions.

The results in Figures 3.6 and 3.7 also demonstrate the reduced influence of discretization when intrinsic dispersion is included in the model. This is evident in the subtle variation of the non-hydrostatic solution versus the transformation of the hydrostatic solution from non-dispersive to dispersive over the range of γ up to 4. The test with the hump diameter $b = 60$ km and grid size $\Delta x = 5.7$ km ($\gamma = 2$), which involves numerical dispersion in both the hydrostatic and non-hydrostatic models, is used to examine manifestation of discretization errors in oblique propagation directions and the concept of effective grid size. Figure 3.8 plots the time series and spectra at 1500 km from the center of the computational grid at $0°$, $22.5°$, and $45°$ relative to the x axis. Numerical dispersion attenuates with wave obliquity in both the hydrostatic and non-hydrostatic solutions resulting in increased attenuation of the trailing waves. The parameter β decreases from 1 to 3/4 as the wave direction turns from the x axis to $22.5°$ and reaches the minimum at 1/2 for propagation along the grid diagonal. The lead-order dispersion relation (43) can be rewritten with the discretization parameter $k(\sqrt{\beta}\Delta x)$ to denote the effective grid spacing. This is supported by the results along the x axis from another set of tests with $\Delta x = 4.94$ and 4.03 km, which correspond to the original grid size of 5.7 km multiplied by $\sqrt{\beta} = \sqrt{3}/2$ and $1/\sqrt{2}$ for waves propagating at $22.5°$ and $45°$. The minor discrepancies are due to interpolation of the surface elevation from adjacent grid points. The use of this effective grid size, which appears to be valid beyond the lead-order approximation, provides an intuitive assessment of numerical dispersion in practical application.

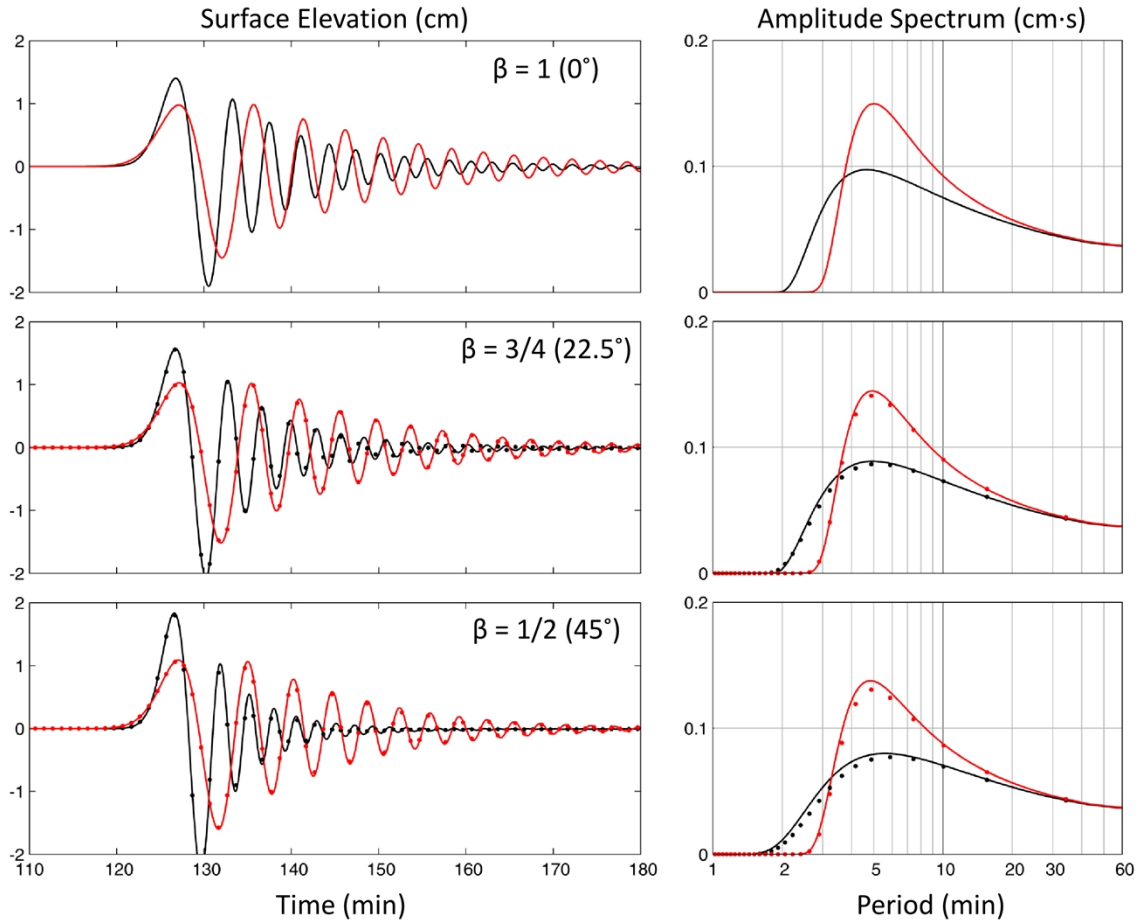Figure 3.8 Time series and spectra at 1500 km from a Gaussian hump with an effective diameter of 60 km at the center. Black and red lines indicate hydrostatic and non-hydrostatic solutions at 0°, 22.5°, and 45° oblique angles for $\gamma = 2$ (Δx = 5.7 km). Black and red dots denote hydrostatic and non-hydrostatic solutions obtained at the x axis using the effective grid spacing $\sqrt{\beta}\Delta x$.

Chapter 4
Case Studies

This chapter is comprised of the materials from the paper "Validation of linearity assumptions for using tsunami waveforms in joint inversion of kinematic rupture models: Application to the 2010 Mentawai Mw 7.8 tsunami earthquake" by Han Yue, Thorne Lay, Linyan Li, Yoshiki Yamazaki, Kwok Fai Cheung, Luis Rivera, Emma M. Hill, Kerry Sieh, Widjo Kongko, and Abdul Muhari that was published in Journal of Geophysical Research: Solid earth in Volume 120, Issue 3, 2015, and the paper "Effects of dispersion in tsunami Green's functions and implications for joint inversion with seismic and geodetic data: a case study of the 2010 Mentawai Mw 7.8 earthquake" by Linyan Li, Kwok Fai Cheung, Han Yue, Thorne Lay and Yefei Bai that was published in Geophysical Research Letters in Volume 43, Issue 21, 2016 .

The intrinsic and numerical dispersion properties have essential influences on wave propagation in non-hydrostatic models and produce waveforms distinct from the hydrostatic results as already demonstrated in the numerical examples in Chapter 3. In this Chapter, effects of dispersion is investigated through finite-fault inversion of the 2010 Mentawai earthquake that involves seismic, geodetic and tsunami data. There are three general approaches to compute tsunami Green's functions for the inversion analysis: hydrostatic and non-hydrostatic modeling with a static initial sea surface pulse derived from seafloor deformation as well as the more accurate non-hydrostatic modeling with kinematic seafloor excitation from the earthquake rupture. The dispersion relation (37) provides insights into the computation and allows quantification of numerical artifacts in the design of the computational grids. NEOWAVE can perform hydrostatic and non-

hydrostatic computations with static or kinematic descriptions of the tsunami source. The use of the same code and nested grid system allows systematic examination of the three types of Green's functions and their influences on the inversion results.

4.1 The 2010 Mentawai Earthquake

The 25 October 2010 *Mw* 7.8 thrust earthquake with epicenter at 3.49°S, 100.14°E ruptured the shallow portion of the Sunda megathrust seaward of the Pagai Islands (see Figure 4.1a for location maps), generating a destructive tsunami that caused more than 500 casualties (Badan Meteorologi, Klimatologi dan Geofisika). Field surveys showed the measured runup is 3-9 m on Pagai and up to 16.9 m on the small island of Sibigau, and the inundation extended more than 300 m at three villages. There was little damage to buildings and infrastructures from the earthquake, because of the less intense ground shaking as indicated from the interviews of local residents (Hill et al., 2012; Satake et al., 2013). The disproportionately large tsunami for the moderate moment magnitude indicates this earthquake was a tsunami earthquake (Kanamori, 1972).

The coseismic rupture process of the 2010 Mentawai event has been investigated using various combinations of seismic, geodetic, and tsunami observations (Bilek et al., 2011; Lay et al., 2011; Newman et al., 2011; Hill et al., 2012; Satake et al., 2013; Yue et al., 2014). Seismic wave investigations resolved an overall northwestward rupture propagation with a low rupture velocity of ~1.5 km/s and a long source duration exceeding 110 seconds (Bilek et al., 2011; Lay et al., 2011; Newman et al., 2011). Localized maximum slip exceeding 4 m near the trench was found by Lay et al. (2011), and this was shown to be consistent with deep-water tsunami observations at a distant DART station, but the spatial resolution was limited. Hill et al. (2012) analyzed regional GPS observations from the Sumatra GPS Array (SuGAr) network and, in reconciling

GPS with tsunami field observations, favored a narrow patch with ~12 m of slip extending 120 km along the shallow fault zone. Satake et al. (2013) inverted tsunami waves observed at 11 sites and performed forward modeling to compare with inundation surveys, finding two localized slip patches with 4-6 m of peak slip near the trench.

The investigations of the rupture process of the 2010 Mentawai earthquake in above studies have established that it was a tsunami earthquake, with large slip on the shallow megathrust. However, there are large differences in inferred slip distributions. Yue et al. (2014) combined SuGAr hr-GPS and teleseismic observations in joint kinematic inversions and iteratively performed forward modeling to fit several tsunami observations, adjusting fault dimensions, rupture velocity, and subfault source time functions to achieve satisfactory fits to all the data. A rupture model with two significant rupture concentrations near the trench was found, with maximum slip much higher (> 20 m) than in other studies. Yue et al. (2015) directly included the tsunami observations in joint inversions to objectively utilize the full information in the tsunami waves. The preferred model indicates a shallow concentration of large slip near the trench with peak slip of ~15 m. The validity of the model is confirmed through fully nonlinear forward modeling of tsunami waveforms for matching the tsunami recordings along with the other data.

The concentrated slip along the trench from the 2010 Mentawai earthquake produced short-period dispersive waves that need to be resolved by tsunami models. The issue becomes more stringent in the inversion analysis due to the need for a detailed finite-fault model. The resulting tsunami Green's functions have to resolve the dispersive waves with even shorter periods generated by the fine subfaults, providing a test case to highlight the interplay between intrinsic and numerical dispersion in practical application.

4.2 Methodology and Data

The joint inversion of the seismic source involves global seismic wave, regional geodetic, and tsunami records. Yue et al. (2015) provided a detailed description of the finite-fault model, the parameterization for the joint inversion, and the recorded geophysical datasets, which include 53 P-wave and 24 SH-wave ground displacements from stations of the Federation of Digital Seismic Networks (FDSNs) and three-component ground motions from 12 high-rate SuGAr GPS stations on the Mentawai Islands maintained by the Earth Observatory of Singapore, Nanyang Technical University. The finite fault model, as illustrated in Figure 4.1b, has 105 subfaults of 15 km by 15 km each, which are arranged in 7 rows along dip and 15 columns along strike. The fine model grid is selected to resolve the concentrated near-trench slip of the tsunami earthquake. The fault has a uniform dip angle of 7.5º based on the shallow megathrust reflection profile of Singh et al. (2011). The source time function of each subfault is parameterized by five triangles with durations of 4 s shifted by 2 s sequentially for a total possible duration of 12 s. The teleseismic Green's functions are generated with a reflectivity method that accounts for interaction in 1-D layered structures on both the source and receiver sides (Kikuchi et al., 1993). A local 1-D layered model based on the reflection imaging is used for the source side and a typical continental model is used for the receiver side. The near-field time-varying ground displacement Green's functions are computed using a frequency-wave number integration method (Hermann, 2013). The same band-pass filter is used for the Green functions and records of each type.

The hydrographic dataset includes tsunami waveforms at two deep-water stations (GITEWS GPS 03 and DART 56001) and two tide gauges at Cocos Island and Padang (see Figure 4.1 for location map). Figure 4.2 plots the recorded waveforms and amplitude spectra. The tsunami recorded at DART 56001, 1600 km from the epicenter, had

relatively simple propagation effects and was recorded in deep water, so the waves are dominated by long-wavelength pulses followed by dispersed and scattered coda. The main pulse provides integral constraints on the slip distribution, but not the spatial details of the slip, as found in earlier studies (Lay et al., 2011; Hill et al., 2012; Satake et al., 2013; Yue et al., 2014). The GPS buoy observations are unusual in being very close to the rupture area (Figure 4.1b), and while they are also in deep water, the signals contain short-period near-field waves that are quite sensitive to the slip distribution and its timing. The tsunami recorded by the Padang tide gauge station traveled through the shallow passages between the Mentawai islands (Figure 4.1b), where the waves were refracted and diffracted. The coda waves in the Padang data include multiple short reflected waves behind headlands, which may be influenced by nonlinearity of the shallow water of less than 8m depth in the bay (Figure 4.1c). The Cocos Island tide gauge recorded even more complex waves in a lagoon of ~12 km diameter and 2 to 5m deep atop an atoll. The coda lasts 4 to 6 times longer than the initial peak due to "ringing" of waves trapped by the island and an adjacent atoll (Figures 4.1d). These four tsunami records sample different propagation characteristics and have varying sensitivity to the slip space-time history, which allows examination of various linearization and dispersion issues.

The NEOWAVE code is used to compute tsunami Green's functions at the four water-level stations for two orthogonal unit slip vectors with 45° and 135° rake to cover displacements in any specific direction determined through the inversion. The two-way nested computational grids allow simultaneous computation of tsunami propagation in the open ocean and transformation at the coast. Dispersion is important for tsunami propagation and is dependent on the intrinsic and numerical properties of the model. The region south of Sunda Strait has an average depth of 5300 m, which requires a grid size of 2.6 and 5.9 arc-m (~4.7 and 10.6 km) to achieve accurate dispersion with $\gamma = 0.8$ and 4

for the non-hydrostatic and hydrostatic computations with a small Courant number. Such grid sizes cannot resolve the many small islands and seamounts in the region that can scatter the tsunami waves influencing the computed Green's functions at the water-level stations. A grid size of 1 arc-m (~1800 m) equivalent to $\gamma = 0.11$ is deemed necessary for the level-1 computation across the Eastern Indian Ocean. While the corresponding non-hydrostatic model overestimates the celerity by 0.3% and 1.1% at $kh = 0.3$ and 0.6, the errors go up to 1.4% and 5.5% for the hydrostatic model (Figure 4.3). The celerity error, which accumulates over time, is typically deemed acceptable with the hydrostatic approach for $kh < 0.3$. This correspond to an error of 1.5% in the absence of dispersion errors. The depth parameters of $kh = 0.3$ and 0.6 correspond to wave periods of 8.2 and 4.3 min for the 5300 m water depth. The hydrostatic model, however, will not be able to adequately resolve wave components shorter than around 8 min. The non-hydrostatic model should be able to describe the harmonic components of the recorded signals shown in Figure 4.2 and the computed Green's function serves as a reference to assess the limitations in the hydrostatic model.

The level-1 grid, which describes tsunami propagation across the open ocean, is locally refined to higher resolution for more detailed processes. A level-2 grid of 12 arc-s (~360 m) is needed to resolve the seafloor deformation generated by the subfaults in the source region around the Mentawai Islands. Telescopic nested grids to level 3 is needed to resolve Cocos Island at 1.5 arc-s (~45 m) and to level 4 for Padang Harbor at 0.3 arc-s (~9 m). The digital elevation model comprises the 30 arc-s (~900m) General Bathymetric Chart of the Oceans from the British Oceanographic Center, the 2 arc-s (~60 m) Digital Bathymetric Model of Badan Nasional Penanggulangan Bencana, Indonesia, 1 arc-s (~30 m) Shuttle Radar Topography Mission from German Aerospace Center, 0.15 arc-s (~5m) lidar data at Padang from Badan Informasi Geospasial, and a 9 arc-s (~270 m) gridded

data set in the Cocos Island region from Geoscience Australia. In addition, the coastal boundaries and nearshore bathymetry at Padang Harbor and Cocos Island are carefully redigitized based on orthoimages and nautical charts. Fixed-wall boundary conditions are imposed on the coastlines and local inundation effects are not modeled in the tsunami Green's functions used in the inversions. The waves reaching Padang pass through the deep channels and should have little effect from overland flow at Pagai shores. In addition, inundation distances on Pagai are short relative to the wavelengths of the tsunami, so effects on the signals at the tide gauge will also be small.

The half-space model of Okada (1992) provides the seafloor deformation for 1-m slip of each subfault and the method of Tanioka and Satake (1996) augments the vertical seafloor motion to account for horizontal displacement on bathymetric slopes. The total vertical displacement defines the static initial sea-surface elevation for computation of the first two sets of Green's functions using the hydrostatic and non-hydrostatic implementations of NEOWAVE. For the third set, the time history of the kinematic seafloor vertical displacement is approximated by a linear function over a 4-s duration to provide a boundary condition for non-hydrostatic modeling of tsunami generation and propagation. Although the hydrodynamic code and tsunami generation mechanism are nonlinear, the seafloor displacement is negligible compared to the water depth and the resulting tsunami amplitude is small even at the Cocos Island lagoon. The computed Green's functions possess the overall linearity required by the inversion routine, but we explore the details for each observing site.

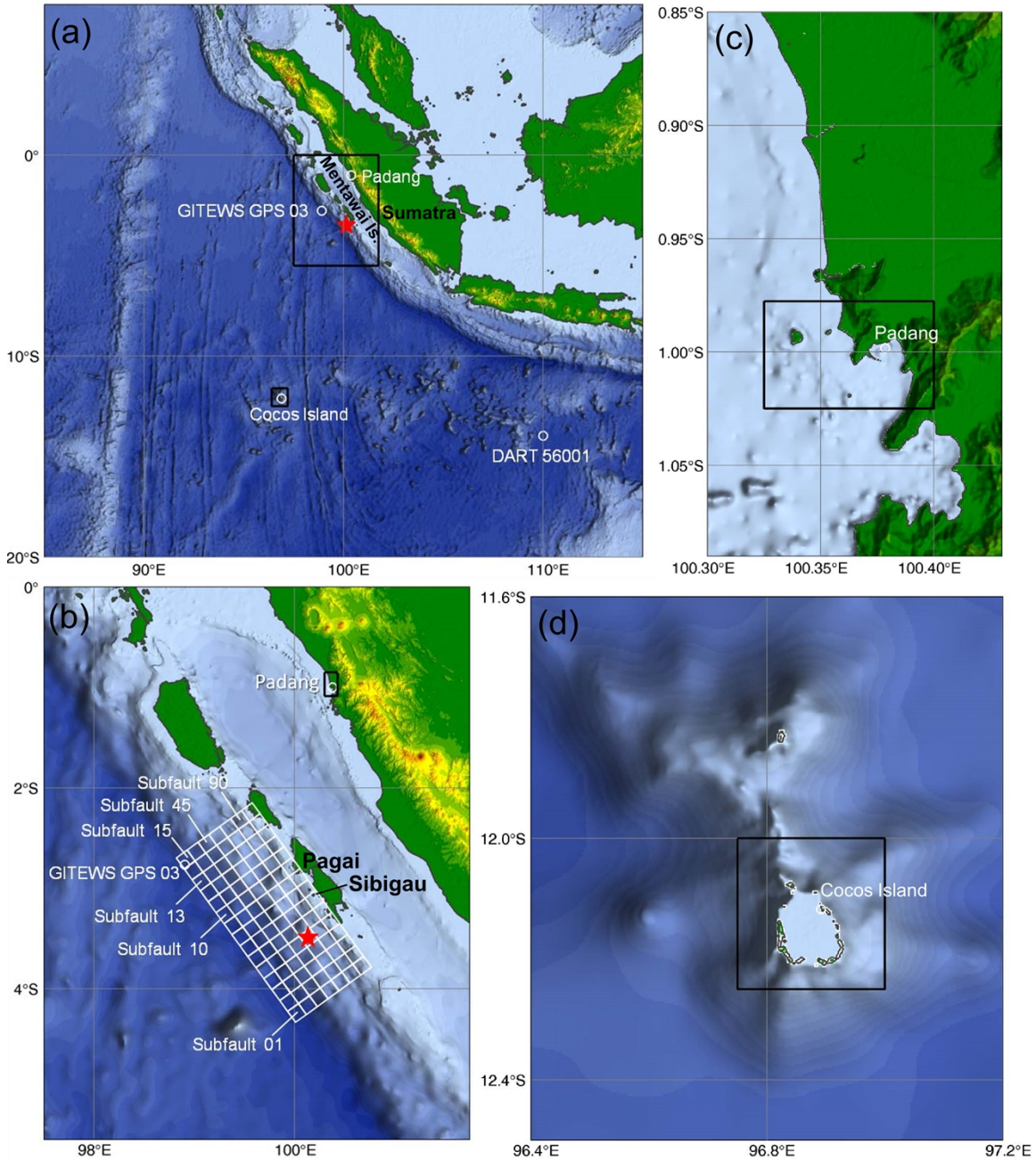Figure 4.1 Location maps and computational grids. (a) Level-1 grid with outlines of level-2 grids around the rupture area and Cocos Island. Red star and white circles indicate the epicenter and water-level stations. (b) Level-2 grid with outlines of level-3 grid at Padang and the source model. (c) Level-3 grid with outline of level-4 grid at Padang Harbor. (d) Level-2 grid with outline of level-3 grid around Cocos Island.
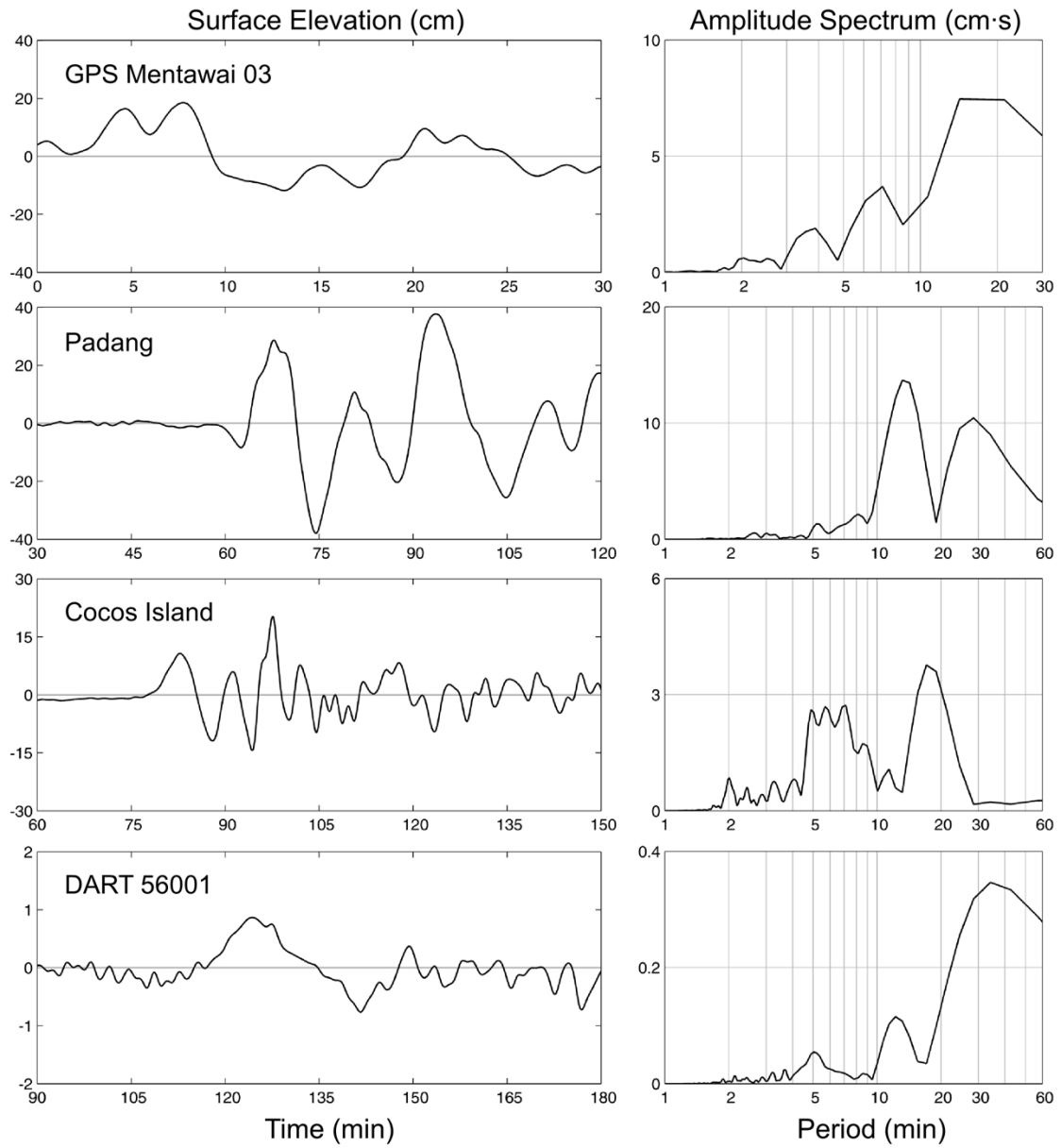
Figure 4.2 Recorded time series of tsunami wave and spectra at the four water-level stations.
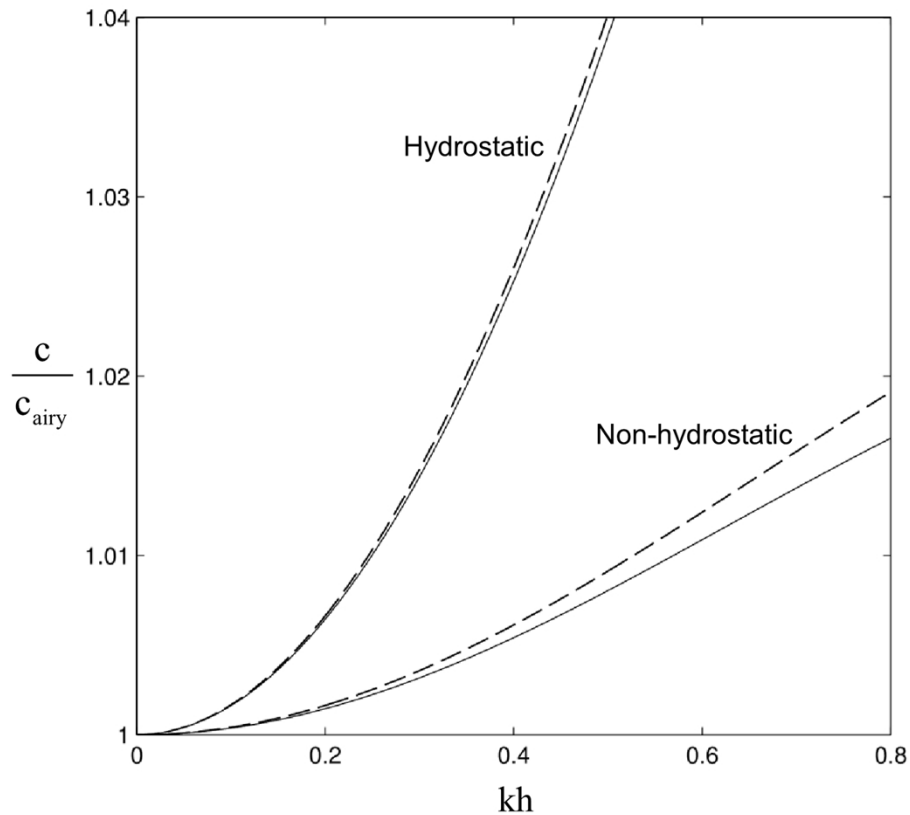
Figure 4.3 Celerity normalized by Airy wave theory as a function of *kh* for hydrostatic and non-hydrostatic models. Solid and dash lines indicate the celerity from the dispersion relation (37) and the intrinsic dispersion relations.

4.3 Dispersion in Tsunami Green's Functions

The 105 subfaults, two slip vectors, four stations, and the three modeling approaches result in 2520 tsunami Green's functions. NEOWAVE generates the Green's functions from kinematic seafloor deformation in contrast to the common approach that utilizes the coseismic seafloor displacement as the initial conditions at the sea surface. The excitation from the seafloor attenuates over the water column and the sea surface has a smaller vertical displacement (Kaijura, 1963; Lay et al., 2013a, 2013b; Li et al., 2015; Bai et al., 2017). Figure 4.4 compares the Green's functions generated by kinematic seafloor deformation and static initial conditions with non-hydrostatic modeling for 1m slip and

46

45° rake at subfaults 8, 11, 13, and 15 along the first row of the model grid (Figure 4.1b). The rise time of 4 s associated with the seafloor deformation has negligible effects on the long-period tsunami waves to enable direct comparison of the two data sets. In Figure 4.4a, the Green's functions at the GPS buoy illustrate their evolution with travel distance. The GPS buoy is located at subfault 15. The smaller initial surface pulse from seafloor excitation is due entirely to the effect during the generation process. In contrast, the large short-period initial pulse from the static initial condition is more dispersive during propagation. By the time when the initial pulse from subfault 8 reaches the GPS buoy, it has the same amplitude as the one generated by seafloor excitation. The larger initial trough and coda are due to more energetic oscillations at the source resulting from free fall of the larger, initial sea surface wave. These source effects are evident at far-field locations such as Padang and Cocos Island as shown in Figures 4.4b and 4.4c. The Green's functions generated by the two approaches are gradually converging and become very similar at the DART buoy 1600 km from the source (Figure 4.4d).

Since effects of the seafloor excitation become more significant as the ratio of the water depth to fault dimension increases (Kaijura, 1963), we utilize the subfaults at different depth to examine its impact on the resulting Green's functions. By including hydrostatic modeling, it provides comparisons among three sets of results to explore the dispersion effects during wave propagation as well. Figure 4.5 plots the maximum surface elevations for unit slip of subfaults 15, 45, and 90 with 45° rake, where their locations extend across the continental slope (Figure 4.1b). The small subfault size presents a challenge to both hydrostatic and non-hydrostatic modeling. The contrast between the three approaches is most pronounced for subfault 15 beneath the trench. The deep water of 5000 m and shallow fault depth of 2.2 km into the rock result in a large ratio of water depth to wavelength, the latter of which is associated with the dimensions

of the seafloor deformation. The absence of direct seafloor excitation and wave dispersion in the hydrostatic approach (H-S) leads to higher estimation of the surface elevation from the source to the far field. The non-hydrostatic approach with the static initial pulse (Nh-S) has the same surface elevation at the source, but produces more rapid amplitude decrease to the far field due to dispersion. Inclusion of kinematic seafloor deformation (Nh-K) accounts for depth-dependent excitation across the water column, resulting in smaller wave amplitude at both the source and in the far field. The tsunami excitation and dispersive wave processes play a lesser role for the deeper subfault 45, which has more spread-out seafloor deformation in shallower water. The three approaches produce very similar results for subfault 90 further down dip, where the water depth is only 500 m and the fault depth is 12.7 km. The small water-depth to wavelength ratio provides an explanation for the minor effects of dispersion in the resulting surface elevation.
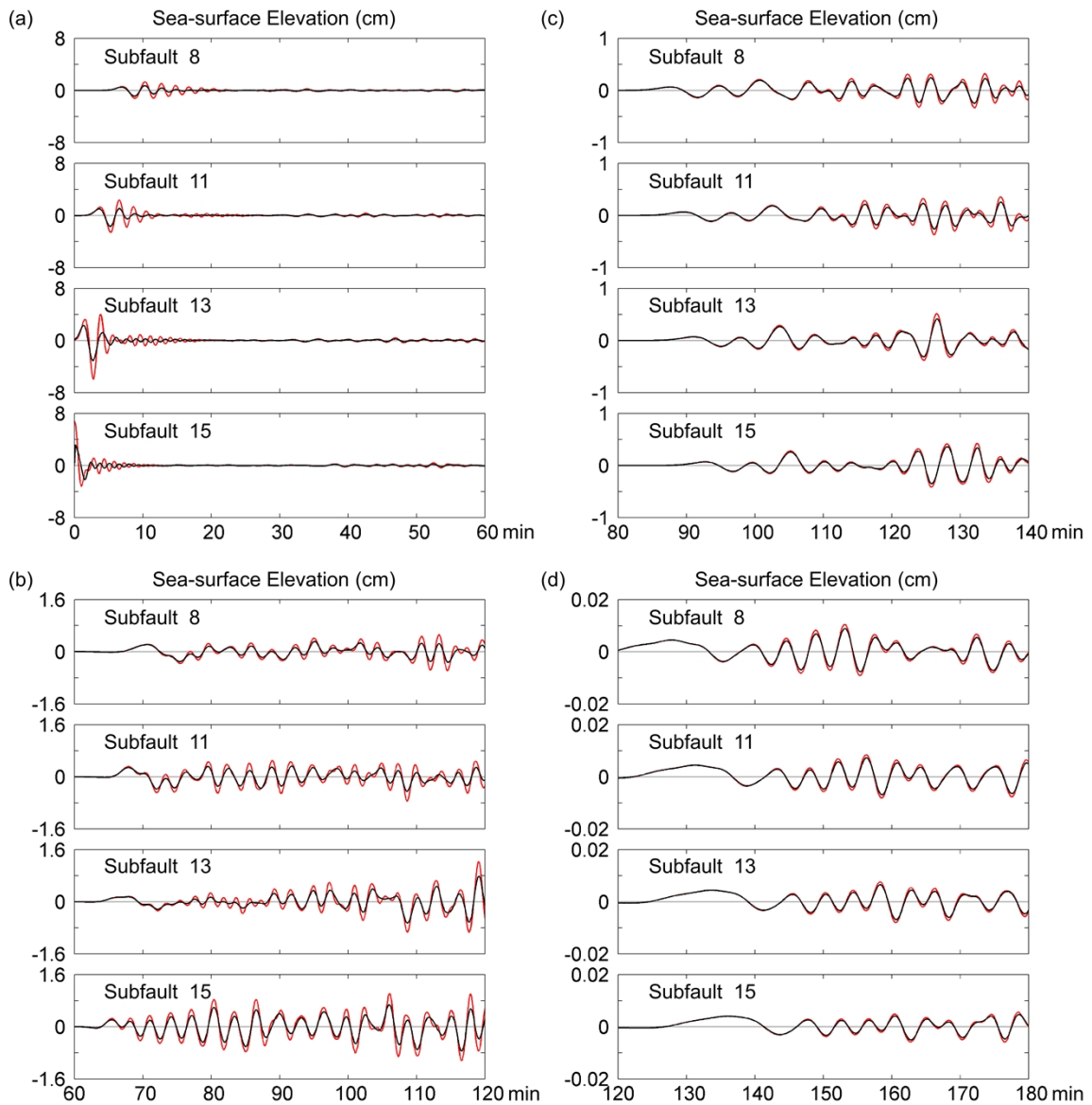
Figure 4.4 Comparison of Green's functions generated by kinematic seafloor deformation with a 4 s rise time (black lines) and static sea surface as initial conditions (red lines). (a) GITEWS GPS. (b) Padang tide gauge. (c) Cocos Island tide gauge. (d) DART 56001. The subfault number refers to the grid in Figure 4.1b, and the Green's functions correspond to 1m slip with 45° rake. The final kinematic seafloor deformation and the static sea surface deformation are identical.

Figure 4.5 Maximum sea-surface elevations generated by the H-S (hydrostatic with static initial sea-surface pulse), Nh-S (non-hydrostatic with static initial sea-surface pulse), and Nh-K (non-hydrostatic with kinematic seafloor excitation) approaches for unit slip of subfaults across the continental slop.
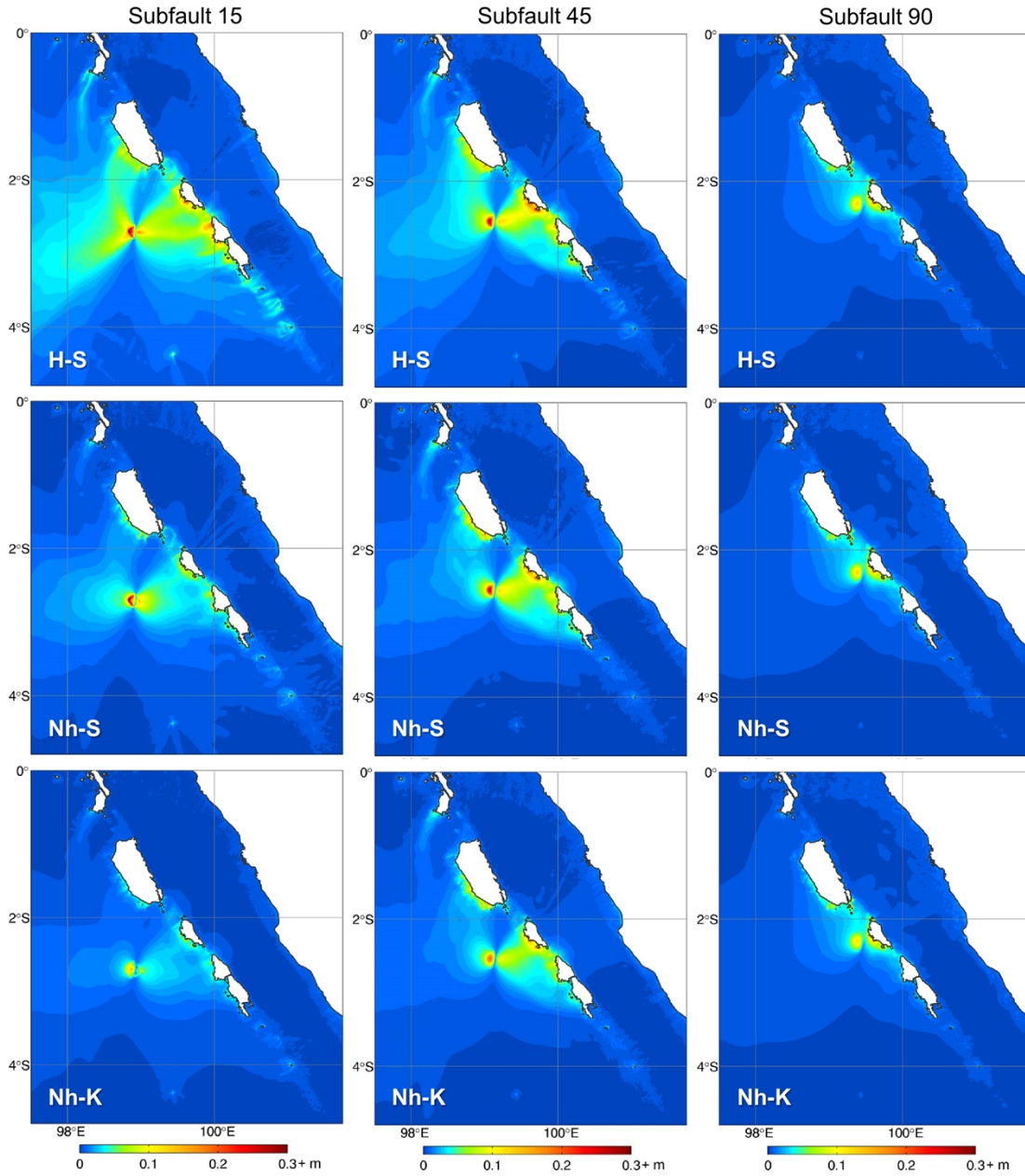
Dispersion influences the waveforms in addition to the amplitude. Figure 4.6 compares the three sets of Green's functions from subfaults 10, 13, 15, 45 and 90 at the four water-level stations. In Figure 4.6a, the Green's functions at the GPS buoy illustrate effects of dispersion in the near field. The buoy is located directly above subfault 15 at the trench, where the seafloor excitation produces a much smaller peak than the initial surface pulse determined from seafloor deformation. Both non-hydrostatic approaches produce oscillations at the source albeit with different phases. The shorter and steeper pulse from the static initial condition is more dispersive. Free fall of the larger, initial sea-surface wave produces more energetic oscillations, but the amplitude attenuates more rapidly in time and space. The phase of the radiated waves approaches that generated by seafloor excitation away from the source as can be inferred from the Green's functions of subfaults 13 and 10 along the trench. The short-period trailing oscillations in the range of dispersive waves are caused by the pointed seafloor uplift from the half-space solution for the shallow subfaults. The Green's functions for subfaults 45 and 90, which are located landward beneath the continental slope, show decreasing dispersion effects due to the shallower water and longer pulse associated with the increasing fault depth. In comparison, the hydrostatic solution shows negligible surface oscillations after the initial upswing even for subfaults 10, 13, and 15 located along the trench.

The Green's functions in the far field reflect mostly the propagation processes. Numerical dispersion is small in both the hydrostatic and non-hydrostatic solutions for the wave period range and grid resolution. At the Padang tide gauge located landward of the source as shown in Figure 4.6b, the two non-hydrostatic approaches produce the same phase from all five subfaults albeit with slightly smaller amplitude obtained with the kinematic seafloor excitation. The hydrostatic approach produces a similar Green's function for subfault 90, but shows increasing discrepancies relative to the non-

hydrostatic predictions for subfaults further up-dip due to the lack of dispersion. The two sets of non-hydrostatic Green's functions show improved agreement of the amplitude away from the source as indicated in the comparisons at Cocos Island and DART 56001 in Figures 4.6c and 4.6d. The waves reaching these two stations have gone through long-distance propagation across the deep ocean. With the exception of subfault 90, the hydrostatic Green's functions show prominent short-period oscillations of 3 min or less due to overestimation of the celerity as observed in the numerical experiments with the Gaussian hump (Figures 3.7). These type of short-period oscillations is commonly seen in tsunami Green's functions computed from small subfaults using hydrostatic models and is routinely removed by filtering.

The non-hydrostatic Green's function based on static initial conditions can serve as a reference to examine the properties and mechanisms of the short-period oscillations from the hydrostatic model. Figure 4.7 compares the hydrostatic and non-hydrostatic Green's functions at the DART buoy generated by unit slip of subfault 10 over a range of grid size from 30 arc-s to 2 arc-m ($\gamma = 0.03$ to 0.46). The shallower fault depth and deeper water down the continental slope together with the fine rupture model result in short-period tsunami signals not adequately resolved by the hydrostatic model. While the non-hydrostatic Green's functions are very similar, the short-period signals in the hydrostatic Green's function are sensitive to the computational grid resolution, as illustrated in Figure 3.3. Filtering removes the numerical oscillations below 3 min period to isolate the tsunami signals observed in the non-hydrostatic solutions as shown in Figure 4.8. The resulting time series indicates simultaneous arrival of long and short-period waves, while the non-hydrostatic solution show lagging of the short-period waves due to lower propagation speeds associated with dispersion.

The short-period signals in the hydrostatic Green's functions are part of the solution from the governing equations in response to overestimation of the celerity. This is normally not an issue for shallow-water waves with $kh < 0.3$. However, the Green's functions correspond to a much larger value of kh because of the small wavelength associated with the subfault. When the Green's functions from all the subfaults are combined, the tsunami signal increases in both amplitude and period with diminishing dispersion effects and short-period oscillations for the larger rupture area as shown in Figure 4.9.
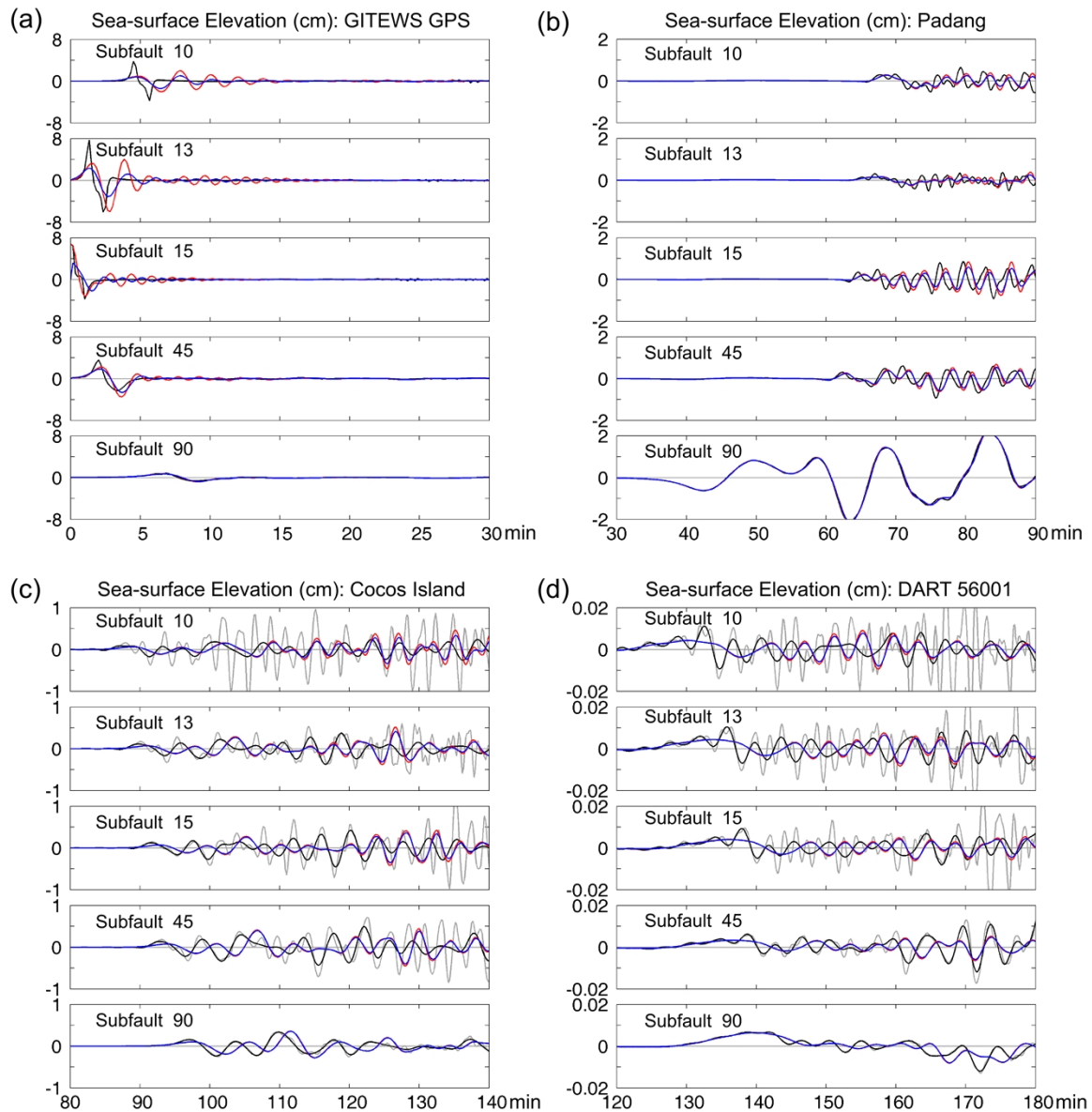
Figure 4.6 Green's functions at (a) GITEWS GPS, (b) Padang, (c) Cocos Island, and (d) DART 56001 generated by the H-S (black), Nh-S (red), and Nh-K (blue) approaches. Kinematic seafloor excitation reduces the initial amplitude at the GITEWS GPS buoy in the near field, but has minor influences in the far-field. Due to limitations of a hydrostatic model in resolving short-period waves, high-frequency numerical oscillations accumulate during propagation. The H-S results at the far-field Cocos Island and DART stations are filtered to remove signals with periods less than 3 min (with the original data shown in grey).

54
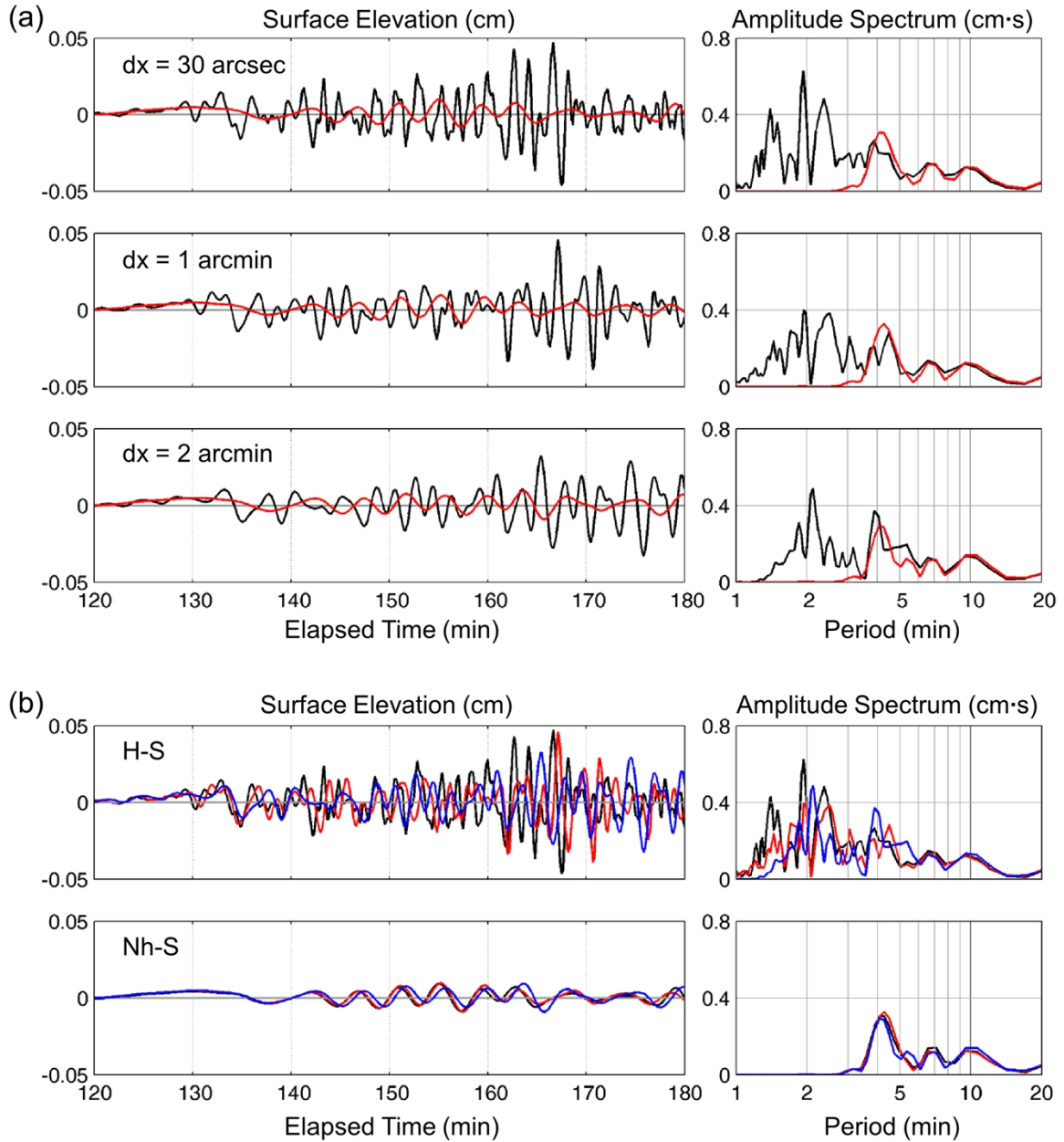
Figure 4.7 Convergence of Green's functions from subfault 10 at DART 56001. (a) Comparison between the H-S (black) and Nh-S (red) approaches. (b) Comparison between grid sizes of 0.5 (black), 1 (red), and 2 (blue) arc-min. The non-hydrostatic Green's functions converge rapidly with the computational grid size. The hydrostatic Green's functions contain the tsunami signals along with short-period oscillations sensitive to the grid size..
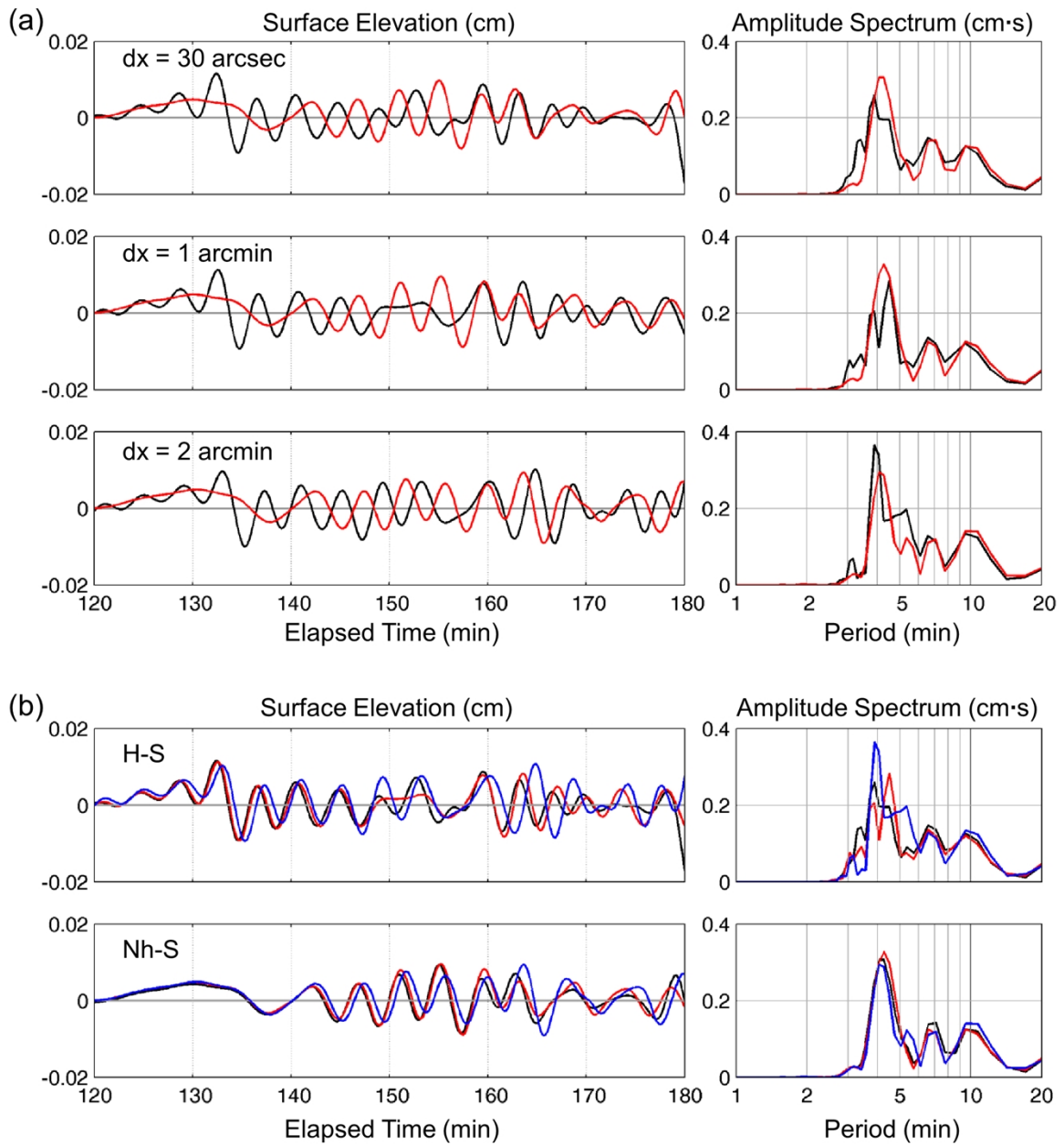
Figure 4.8 Convergence of Green's functions from subfault 10 at DART 56001 with filtering of the hydrostatic results to remove signals below 3 min period. (a) Comparison between the H-S (black) and Nh-S (red) approaches. (b) Comparison between grid sizes of 0.5 (black), 1 (red), and 2 (blue) arc-min. The hydrostatic Green's functions show tsunami signals over a wide period range arriving simultaneously at the station due to the lack of dispersion.
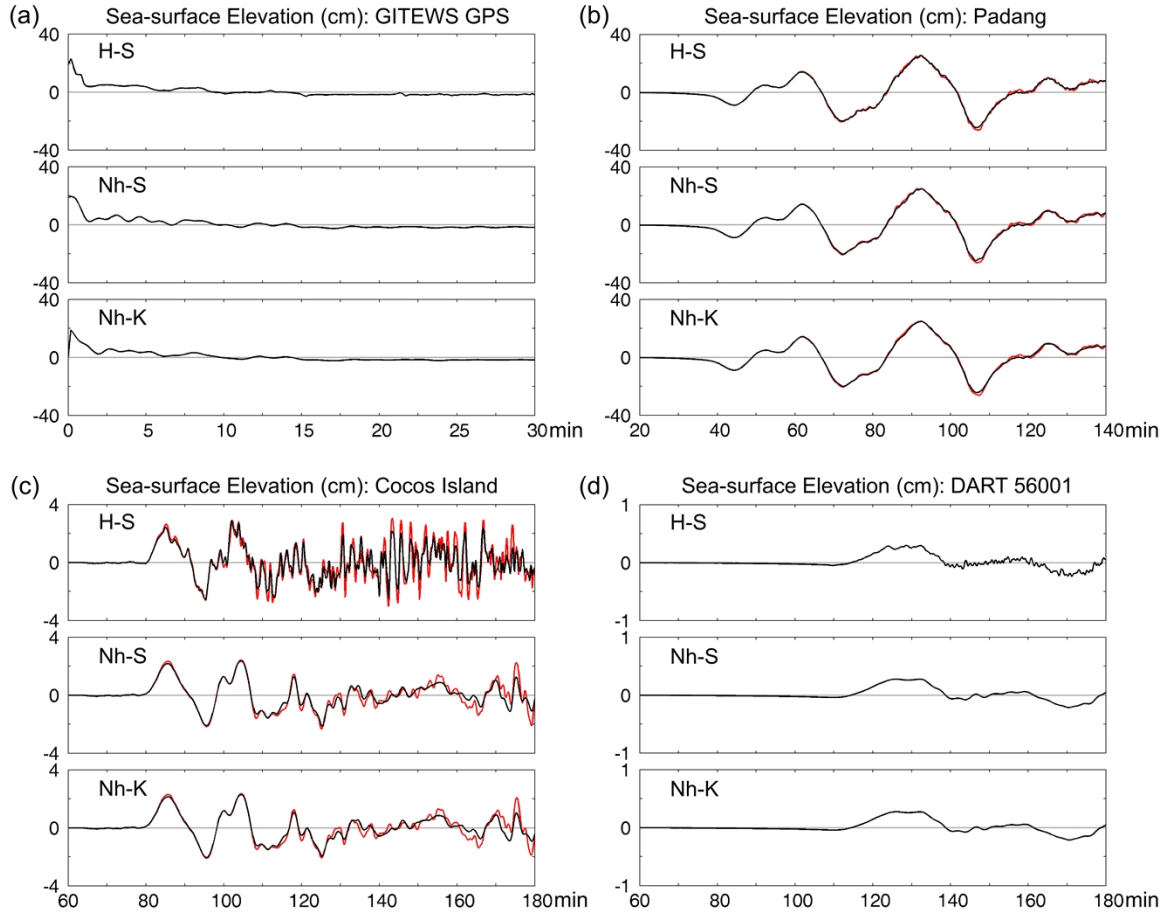
Figure 4.9   Comparison between linearly combined Green's functions (red lines) from all 105 subfaults and NEOWAVE output (black lines) at the four water-level stations (a) through (d) from the H-S, Nh-S, and Nh-K approaches. The minor discrepancy between the superposed Green's functions and the NEOWAVE output at Cocos Island is related to nonlinearity over the shallow lagoon. The numerical oscillations in the hydrostatic results are reduced through the superposition due to longer period waves from a larger rupture area.

4.4 Superposition of Tsunami Green's Functions

The principle of inversion analysis is based on superposition of precomputed Green's functions to reconstruct observed signals. Linearity is implicit in kinematic rupture process inversions. The present application involves staggering of the Green's functions in time to mimic the rupture propagation, the use of the two orthogonal components to resolve the local rake angle, and scaling of dispersion properties through superposition of slips on different subfaults. A series of tests involving the non-hydrostatic Green's

57

functions based on kinematic seafloor deformation provide assessment of these superposition processes.

Figure 4.10a compares the linearly scaled Green's function and the full NEOWAVE computation for 10 m slip at subfault 37 with 4 s rise time and 45° rake. Subfault 37 is in the middle of the rupture area representative of the overall characteristics. Both sets of results are nearly identical at the GPS and DART buoys due to linearity of tsunami waves in the deep ocean. The discrepancy in the short-period codas at the Padang and Cocos Island tide gauges likely arises from nonlinear effects in shallow water. Figure 4.10b shows results using the same slip and rake at subfault 37, but with a 40 s rise time. The Green's function, which corresponds to 1m slip and 4 s rise time, is shifted and summed at 4 s intervals to mimic the 10 m slip over 40 s. The results are almost identical to those linearly scaled from the Green's function as shown in Figure 4.10a. The comparison of the nonlinear results between the two cases confirms that the waveforms are relatively independent of the rise time up to 40 s. The minor phase shift introduced by the 40 s rise time has negligible effects on the computed tsunami with periods of over 10 min.

The finite-faulting inversion routine resolves variable rake at each subfault by using a pair of Green's functions computed for unit slip with distinct rakes; for the tests here we use 45° and 135°. Figure 4.10c shows that the linearly combined Green's functions from the two orthogonal components at subfault 37 are nearly identical to the NEOWAVE results computed for 90° rake with the same resultant slip and rise time. The agreement at the Padang and Cocos Island tide gauges are much improved compared to the earlier tests because of negligible nonlinear effects associated with the much smaller wave amplitude. The final test involves uniform 1 m slip of the entire rupture grid for 45° rake and 4 s rise time. The results from the linear superposition and the full NEOWAVE computation in Figure 4.10d show very good agreement. The large fault dimensions compared to the

water depth result in minimal oscillations at the source after the initial pulse in accordance to long-wave theory. The linearly combined Green's functions are able to reproduce the increased wave periods due to the large fault area and subsequent arrival or development of shorter-period waves at the far-field water level stations. Linearity holds up well for the two deep ocean tsunami records (GPS buoy and DART 56001) and the results are consistent with expectations for deep ocean records. For the Padang and Cocos tide gauge records, the nonlinear effect is apparent for the coda waves, consistent with their generation by reflection near the coasts, where nonlinear effects are expected to be significant. For the initial peaks of the records, which are used in the finite-fault inversion, linearity is valid.
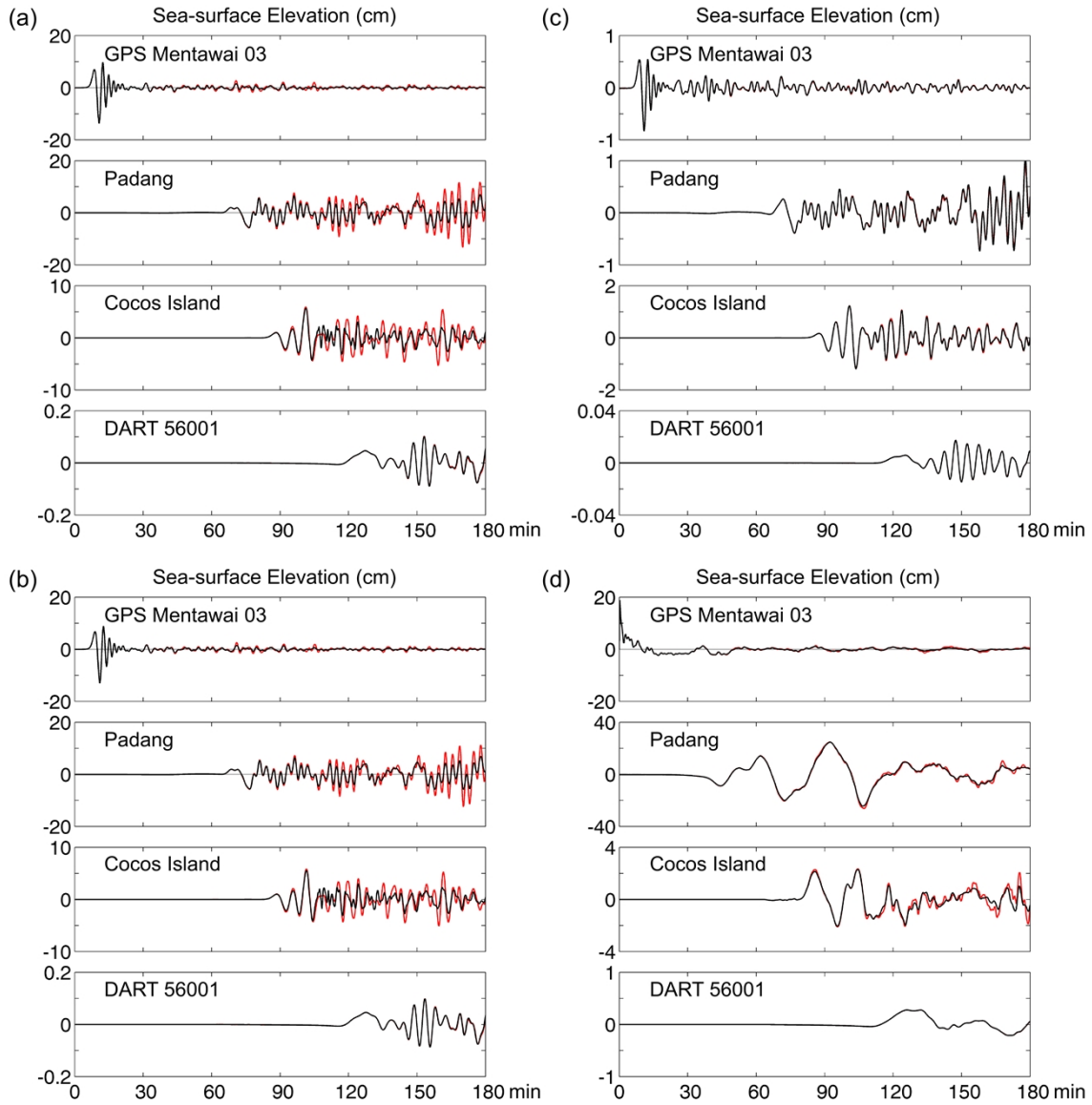
Figure 4.10 Comparison of linearly combined Green's functions for 1 m slip (red dashed lines) with full-scale NEOWAVE output (black lines) for (a) 10m slip at subfault 37 with 4 s rise time and 45° rake, (b) 10 m slip at subfault 37 with 40 s rise time and 45° rake, (c) 1 m slip at subfault 37 with 4 s rise time and 90° rake, and (d) 1 m slip at all subfaults with 4 s rise time and 45° rake.

4.5 Results and Discussion

This study use the same datasets of the 2010 Mentawai M_W 7.8 earthquake from Yue et al. (2015) to examine the sensitivity of finite fault inversion to the three types of tsunami Green's functions with varying degree of dispersion effects. The P and SH waves are sampled at 0.5 s intervals over a 120-s window starting 10 s prior to arrivals. Each trace of the Hr-GPS records has a 200-s window sampled at 1-s intervals starting at the origin time of the hypocenter. The recorded tsunami arrivals at the Padang and Cocos Island tide gauges are 2 and 4 min ahead of the model results and are shifted accordingly to offset the timing discrepancy, which we attribute to bathymetric inaccuracies. The recorded waveforms, which have varying amplitudes among the four stations, are adjusted by scaling parameters to achieve consistent weights in the inversion. When the filtered hydrostatic Green's functions at Cocos Island and DART 56001 are used in the inversion, the corresponding records are filtered in the same way to avoid projection of any artifacts into the solution. A rupture velocity of 2.0 km/s expanding from the hypocenter defines the rupture initial time at each subfault. The finite-fault inversion involves solving for space-time varying weights of the Green's functions to match the recorded datasets through a non-negative linear least squares approach.

Figure 4.11 compares the observed and predicted waveforms at the four water-level stations from the tsunami-only and joint inversions using the non-hydrostatic Green's functions with static and kinematic seafloor deformation as well as the hydrostatic Green's functions with and without filtering. The inversion time windows include the initial double peaks at the GPS buoy, the first two waves at Padang and Cocos Island, and the dominant long-period pulse at the DART buoy. The waveforms in these time intervals provide information most relevant to the source. The overall fits within the time windows are quite good. The various types of Green's function produce similar results despite their

varying waveforms at the stations. As long as the model representation has sufficient degrees of freedom, the least squares approach can produce a good fit to the observations with the variations among the Green's functions compensated by the source model. The short-period oscillations in the hydrostatic Green's functions do not appear to interfere with the fitting of the tsunami signals, but do show up subsequently in the predicted waveforms. The discrepancy between the recorded and predicted waveforms also increases outside the inversion time windows. The two sets of non-hydrostatic Green's functions maintain very similar predictions, while the filtered hydrostatic Green's functions produce comparable amplitude with a notable phase shift. The joint inversion results show slightly larger deviations from the records due to the intrinsic need to reconcile multiple datasets that might not be fully compatible.

The inversions provide the slip distributions shown in Figure 4.12. All slip models involve primary rupture propagation up dip and along strike in the northwest direction. The detailed slip distribution varies significantly with the type of Green's functions used in the inversion despite the similar fits to the tsunami observations. For the tsunami-only inversion in Figure 4.12a, the non-hydrostatic Green's functions resolve the large concentrated slip extending along the trench. The model with kinematic seafloor excitation has maximum slip of 15.9 m, while the static initial condition results in a lower value of 13.6 m as needed to account for the absence of wave attenuation at the source. Filtering is necessary for the hydrostatic Green's functions that have increasing numerical oscillations for subfaults near the trench. The alignment of the frequency components due to the lack of dispersion is compensated by a more spread-out slip distribution and a further reduction of the maximum slip to 10.0 m. Without filtering, the inversion suppresses the numerical oscillations to fit the recorded waveforms by spreading the slip more evenly down dip. This results in relatively small slip of less than 5.8 m near the

trench. The cumulative seismic moments for the four predictions are still close, in the range of 8.9 to 9.2×10^{20} Nm (M_W 7.90-7.91).

The results from the joint inversion in Figure 4.12b show similar effects of the tsunami Green's functions, but with more focused slip distributions along the trench (see Figures 4.13 and 4.14 for sample comparisons of geodetic and seismic datasets). The inversions with non-hydrostatic Green's functions produce maximum slip of 15.7 and 13.3 m comparable to the tsunami-only inversions. In the absence of dispersion in the tsunami Green's functions, the seismic and geodetic datasets play a more significant role in defining the slip along the trench. The joint inversion gives maximum slip of 8.4 m when the filtered Green functions are used. When the near-trench slip is suppressed and spread down dip through the use of the unfiltered hydrostatic Green's functions, the geodetic and seismic datasets help maintain the maximum slip at 7.1 m. The cumulative moments of $7.5\text{-}8.3 \times 10^{20}$ Nm (M_W 7.85-7.88) are consistently lower than those of the tsunami-only inversions indicating reconciliation among the tsunami, geodetic, and seismic datasets through the inversion process.
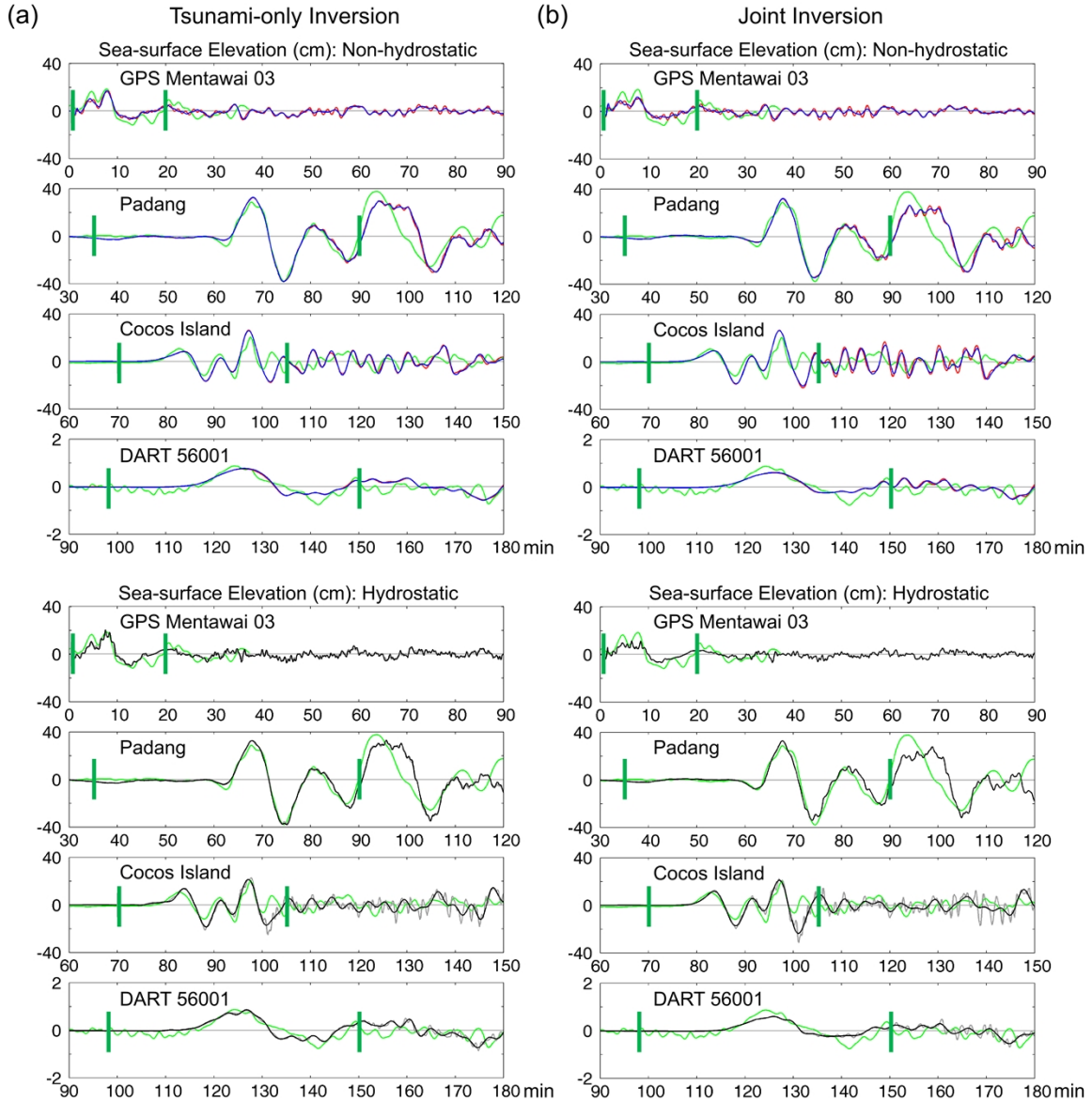
Figure 4.11 Tsunami waveform comparison for (a) tsunami-only and (b) joint inversions. Green lines denote recorded data, red and blue lines indicate computed waveforms from the Nh-S and Nh-K approaches, and black and grey are the H-S Green's functions with and without filtering. The vertical bars identify time windows of tsunami records used in the inversions.
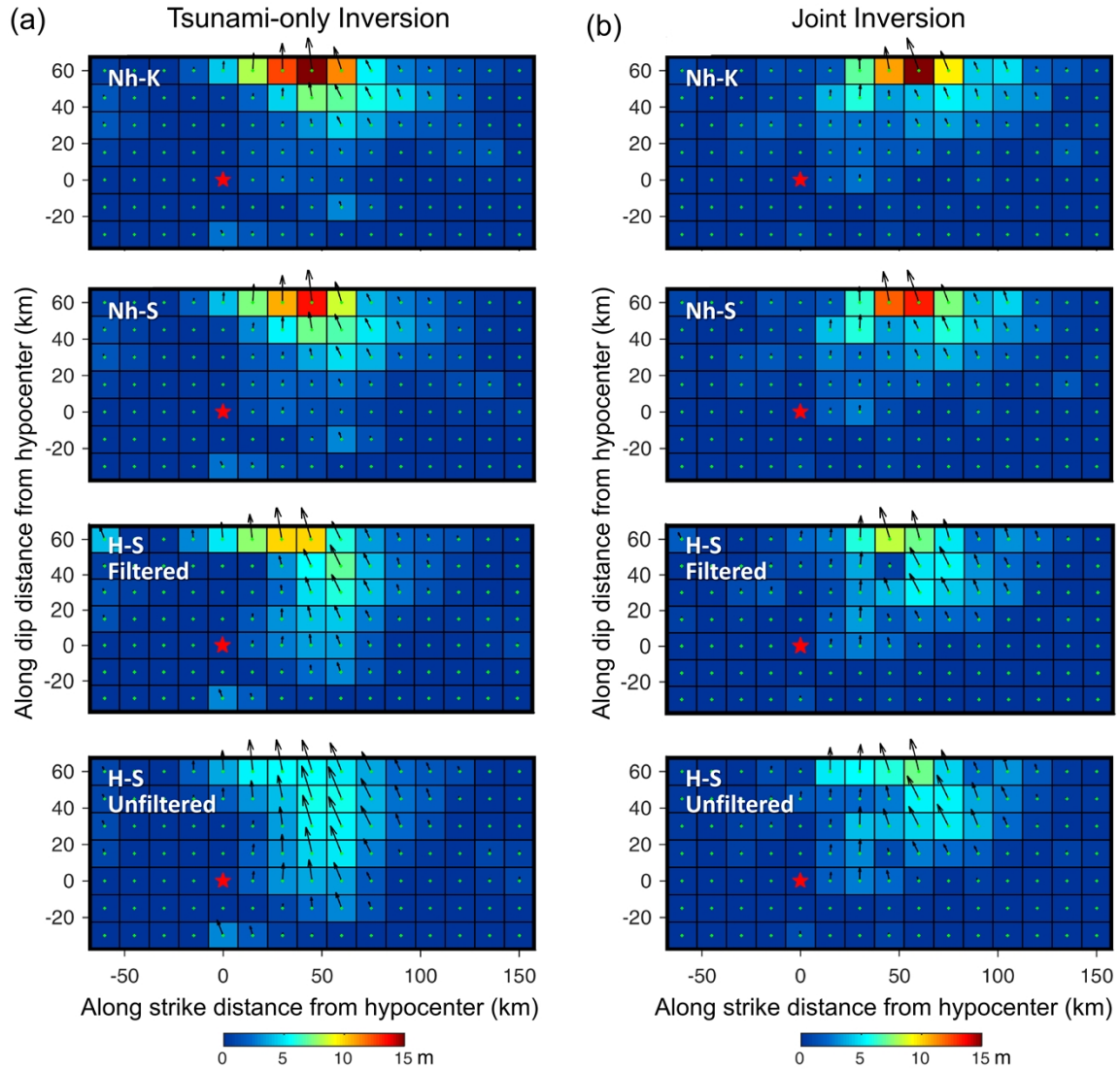
Figure 4.12 Slip distributions on the fault model grid inverted using tsunami Green's functions generated by the Nh-K, Nh-S, and H-S (filtered and unfiltered) approaches. (a) Tsunami-only inversion. (b) Joint inversion. Green's functions from non-hydrostatic modeling are necessary to resolve the large, concentrated near-trench slip consistent with the geodetic and seismic datasets.

E Comp　　　　　　　　　　**N Comp**

mnna Δ=322 km Φ=109 °

trtk 226 14

ngng 211 333

lais 210 91

lnng 175 40

pkrt 163 336

mkmk 149 45

ktet 130 345

smgy 97 358

slbu 82 350

prkb 65 26

bsat 49 19

0　　50　　100　　150　　0　　50　　100　　150

Time (s)

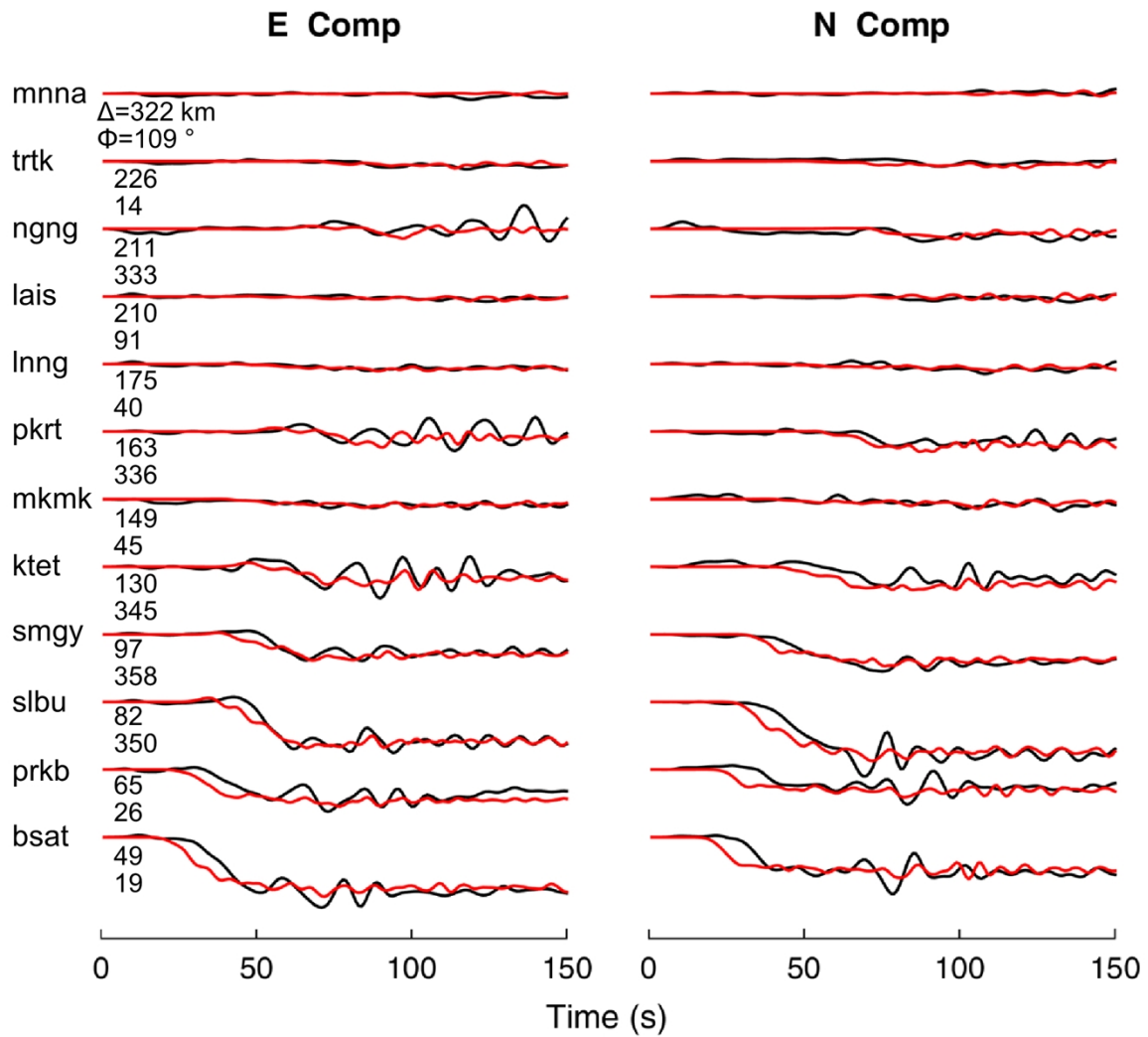Figure 4.13   Horizontal components of recorded (red) and modeled (black) hr-GPS ground displacement signals from the joint inversion with the tsunami Green's functions from the Nh-K approach. The stations are ordered by epicentral distance.
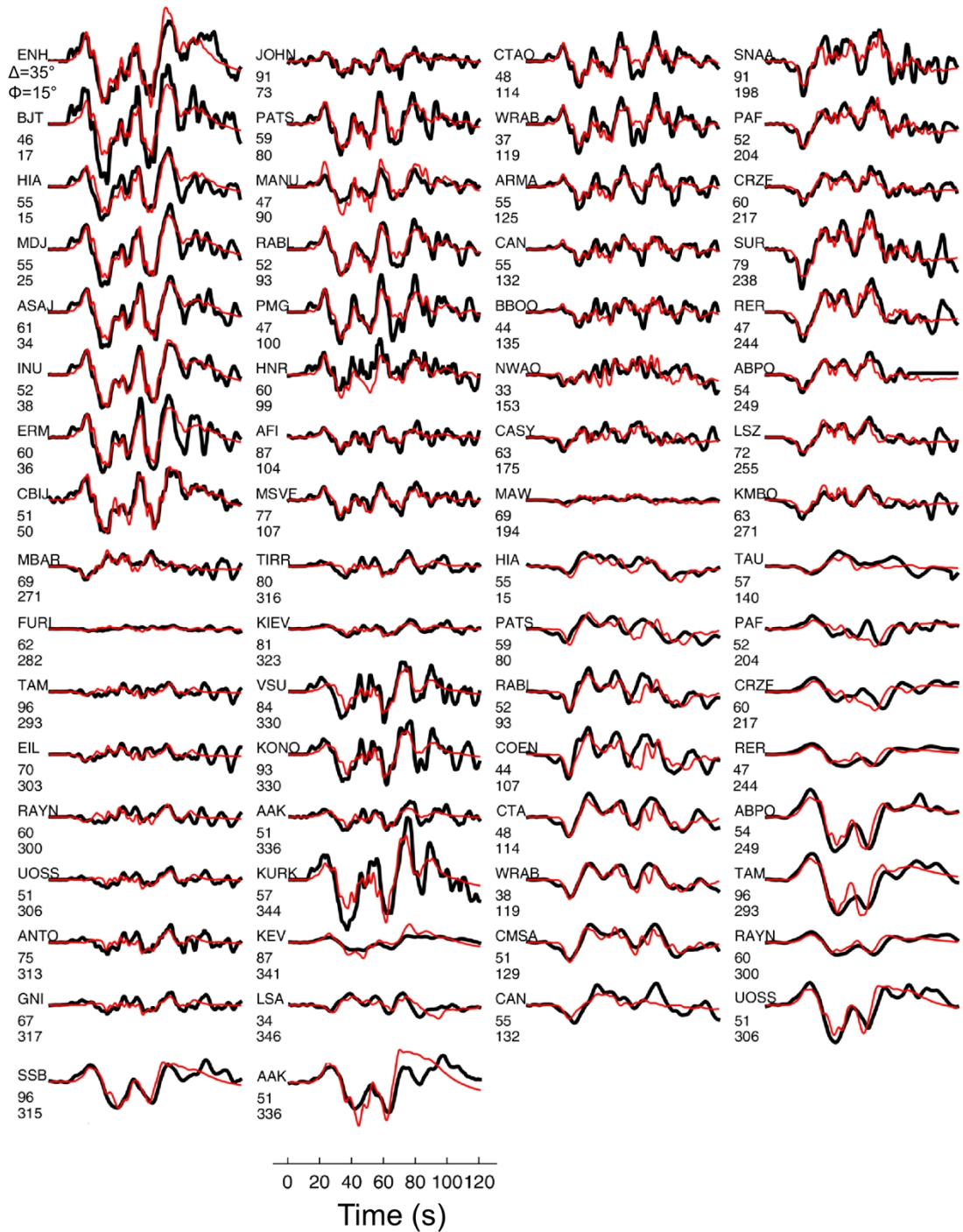
Figure 4.14 Recorded (red) and modeled (black) teleseismic waves from the joint inversion with the tsunami Green's functions from the Nh-K approach. The stations are ordered by azimuth.

67

Chapter 5
Conclusions

The Fourier method is effective and straightforward in deriving exact dispersion relations for numerical wave models from the eigenvalue of the discretized governing equations. The extension of the method from hydrostatic to non-hydrostatic models simply increases the rank of the eigenvalue matrix from three to five. The staggered finite-difference scheme remains non-dissipative with inclusion of the non-hydrostatic terms through the Keller-box scheme in the vertical direction. The eigenvalue gives rise to a combined relation for intrinsic and numerical dispersion with the latter manifested as a phase error associated with the spatial and temporal discretization. The dispersion relation is independent of the semi-implicit scheme for the solution of the non-hydrostatic terms. Introduction of Taylor expansions produces a lead-order approximation, which demonstrates the interrelationship among the depth and discretization parameters in modulating dispersion.

The exact and lead-order dispersion relations provide insights into the interplay between intrinsic and numerical dispersion during the computation and an useful tool to select discretization parameters as demonstrated by the numerical experiments. The depth and spatial discretization parameters have complementary effects on dispersion providing a means to optimize numerical wave models through adjustment of the grid size. Their coupling, however, results in notable reduction of numerical dispersion outside the shallow-water range. The temporal discretization tends to reduce numerical dispersion, but is secondary within the range of Courant numbers used in wave modeling. Numerical dispersion, which results primarily from truncation errors associated with the spatial discretization, decreases for oblique wave propagation due to effective increase in resolution and reaches a minimum at 45° from a principal axis of the grid.

68

Discretization errors in shallow-water equations can mimic dispersion from Boussinesq-type or non-hydrostatic systems for tsunami modeling, but the required grid size might not be sufficient to resolve the many seamounts and islands across the Pacific. The Boussinesq-type equations, which already have accurate description of dispersion in the tsunami range, might be adversely affected by numerical dispersion. On the other hand, the Keller box scheme results in underestimation of dispersion by the governing equations of non-hydrostatic models. The spatial discretization errors can be tuned to offset the underestimation to better describe trans-Pacific propagation of tsunamis. A tsunami consists of a number of harmonics related to the complexity of the seafloor deformation at the source. The components with varying dispersion properties need to be captured by a computational grid spanning across the ocean. The use of a 2-arcmin grid is optimal in balancing intrinsic and numerical dispersion over a wide range of water depth parameters in the non-hydrostatic model.

Dispersion effects are most evident in finite-fault inversion of tsunami signals due to the use of small subfaults to resolve seafloor deformation. The dispersion relation derived in this study allows assessment of the discretization errors in further influencing the numerical solution. This has been demonstrated by the slip distributions of the 2010 Mentawai earthquake inverted using the three types of tsunami Green's functions. The results differ significantly even though they have comparable total seismic moments and similar fits to the tsunami recordings. This makes it difficult to assess the validity of source models from the predicted waveforms and therefore emphasizes the need to properly account for tsunami generation and dispersion processes. The Green's functions computed using a non-hydrostatic model with either kinematic seafloor excitation or static initial conditions improve resolution of concentrated near-trench slip. Depth-dependent tsunami excitation influences the amplitude and phase of the Green's functions

close to the source, providing better resolution of the slip when near-field observations are available.

Assumption of the initial sea surface elevation based on coseismic seafloor deformation is implicit in the Green's functions generated by the hydrostatic approach. The shallow fault depth near the trench results in short-period waves generated in relatively deep water. The hydrostatic model overestimates the initial wave amplitude from seafloor displacement, forces the harmonic components to remain aligned during propagation, and introduces short-period oscillations due to overestimation of the celerity. In matching the tsunami recordings, the inversion acquires an excessively smoothed slip distribution to suppress the short-period oscillations in the Green's function. Even with filtering, the hydrostatic Green's functions still produce spread-out, lower amplitude slip to compensate for the lack of dispersion. Non-hydrostatic tsunami calculations are clearly warranted for reliable imaging of detailed slip distributions.

References

Abbott, M. B., McCowan, A. D., Warren, I. R., 1984. Accuracy of short-wave numerical models. J Hydraulic Eng. 110(10), 1287–1301. doi:10.1061/(ASCE)0733-9429(1984)110:10(1287).

Bai, Y., Cheung, K. F., 2013. Depth-integrated free-surface flow with parameterized non-hydrostatic pressure. Int. J. Numer. Meth. Fluids 71(4), 403–421. doi:10.1002/fld.3664.

Bai, Y., Cheung, K. F., 2016. Linear and nonlinear properties of reduced two-layer models for non-hydrostatic free-surface flow. Ocean Modell. 107, 64–81. doi: 10.1016/j.ocemod.2016.10.003.

Bai, Y., Lay, T., Cheung, K. F., Ye, L., 2017. Two regions of seafloor deformation generated the tsunami for the 13 November 2016, Kaikoura, New Zealand earthquake. Geophys. Res. Lett. 44, 6597–6606. doi: 10.1002/2017GL073717.

Bai, Y., Yamazaki, Y., Cheung, K. F., 2018. Convergence of multilayer nonhydrostatic models in relation to boussinesq-type equations. J. Waterw. Port Coast. Ocean Eng. 144(2). doi: 10.1061/(ASCE)WW.1943-5460.0000438.

Bricker, J. D., Munger, S., Pequignet, C., Wells, J. R., Pawlak, G., Cheung, K. F., 2007. ADCP observations of edge waves off Oahu in the wake of the November 2006 Kuril Islands tsunami. Geophys. Res. Lett. 34(23). doi:10.1029/2007GL032015.

Burwell, D., Tolkova, E., Chawla, A., 2007. Diffusion and dispersion characterization of a numerical tsunami model. Ocean Modell. 19(1), 10–30. doi:10.1016/j.ocemod.2007.05.003.

Bilek, S. L., Engdahl, E. R., DeShon, H. R., Hariri, M. El, 2011. The 25 October 2010 Sumatra tsunami earthquake: Slip in a slow patch. Geophys. Res. Lett. 38(14). doi:10.1029/2011GL047864.

Cho, Y.-S., 1995. Numerical simulations of tsunami propagation and run-up. Ph.D. thesis. Cornell University.

Cho, Y.-S., Sohn, D.-H., Lee, S. O., 2007. Practical modified scheme of linear shallow-water equations for distant propagation of tsunamis. Ocean Eng. 34(11), 1769–1777. doi: 10.1016/j.oceaneng.2006.08.014.

Foreman, M. G. G., 1984. A two-dimensional dispersion analysis of selected methods for solving the linearized shallow water equations. J. Comput. Phys. 56(2), 287–323. doi: 10.1016/0021-9991(84)90097-4.

Gobbi, M. F., Kirby, J. T., Wei, GE, 2000. A fully nonlinear Boussinesq model for surface waves. Part 2. Extension to $O(kh)^4$. J. Fluid Mech. 405, 181–210. doi: 10.1017/S0022112099007247.

Ha, T., Cho, Y.-S., 2015. Tsunami propagation over varying water depths. Ocean Eng. 101, 67–77. doi: 10.1016/j.oceaneng.2015.04.006.

Hanson, J. A., Bowman, J. R., 2005. Dispersive and reflected tsunami signals from the 2004 Indian Ocean tsunami observed on hydrophones and seismic stations. Geophys. Res. Lett. 32(17). doi: 10.1029/2005GL023783.

Herrmann, R. B. 2013. Computer programs in seismology: An evolving tool for instruction and research. Seism. Res. Lett. 84, 1081-1088. doi:10.1785/0220110096.

Hill, E. M., et al., 2012. The 2010 M_W 7.8 Mentawai earthquake: Very shallow source of a rare tsunami earthquake determined from tsunami field survey and near-field GPS data. J. Geophys. Res. 117. doi:10.1029/2012JB009159.

Horrillo, J., Kowalik, Z., Shigihara, Y., 2006. Wave dispersion study in the Indian Ocean-Tsunami of December 26, 2004. Mar. Geod. 29(3), 149–166. doi: 10.1080/01490410600939140.

Hossen, M. J., Cummins, P. R., Dettmer J., Baba T. 2015. Tsunami waveform inversion for sea surface displacement following the 2011 Tohoku earthquake: Importance of dispersion and source kinematics, J. Geophys. Res. Solid Earth 120, 6452–6473. doi:10.1002/2015JB011942.

Imamura, F., Shuto, N., Goto, C., 1988. Numerical simulations of the transoceanic propagation of tsunamis, in Sixth Congress of the Asian and Pacific Regional Division, Int. Assoc. Hydraul. Res., Kyoto, Japan.

Kirby, J. T., Shi, F., Tehranirad, B., Harris, J. C., Grilli, S. T., 2013. Dispersive tsunami waves in the ocean: Model equations and sensitivity to dispersion and Coriolis effects. Ocean Modell. 62, 39–55. doi: 10.1016/j.ocemod.2012.11.009.

Kaijura, K., 1963. The leading wave of a tsunami. Bull. Earthquake Res. Inst. 41, 535–571.

Kowalik, Z., Bang, I., 1987. Numerical computation of tsunami run-up by the upstream derivative method. Sci. Tsunami Haz. 5(2), 77–84.

Kulikov, E., 2006. Dispersion of the Sumatra tsunami waves in the Indian Ocean detected by satellite altimetry. Russ. J. Earth Sci. 8. doi: 10.2205/2006ES000214.

Kanamori, H., 1972. Mechanism of tsunami earthquakes, Phys. Earth Planet. Inter. 6, 346–359. doi:10.1016/0031-9201(72)90058-1.

Kikuchi, M., Kanamori, H., Satake, K., 1993. Source complexity of the 1988 Armenian earthquake: Evidence for a slow after-slip event. J. Geophys. Res. 98(B9), 15,797–15,808. doi:10.1029/93JB01568.

Leendertse, J. J., 1967. Aspects of a computational model for long-period water-wave propagation. Report RM-5294-PR, The Rand Corp., Santa Monica.

Li, L., Lay, T., Cheung, K. F., Ye, L., 2015. Joint modeling of teleseismic and tsunami wave observations to constrain the 16 September 2015 Illapel, Chile, Mw 8.3 earthquake rupture process. Geophys. Res. Lett. 43, 4303–4312. doi:10.1002/2016GL068674.

Li, L., Cheung, K. F., Yue, H., Lay, T., Bai, Y., 2016. Effects of dispersion in tsunami Green's functions and implications for joint inversion with seismic and geodetic data: A case study of the 2010 Mentawai Mw 7.8 earthquake. Geophys. Res. Lett. 43, 11,182–11,191. doi: 10.1002/2016GL070970.

Liu, P. L.-F., Cho, Y.-S., Briggs, M. J., Kanoglu, U., Synolakis, C. E., 1995. Runup of solitary waves on a circular island. J. fluid mech. 302, 259–285. doi: 10.1017/S0022112095004095.

Lay, T., Ammon, C. J., Kanamori, H., Yamazaki, Y., Cheung, K. F., Hutko, A. R., 2011. The 25 October 2010Mentawai tsunami earthquake (Mw 7.8) and the tsunami hazard presented by shallow megathrust ruptures. Geophys. Res. Lett. 38(6). doi:10.1029/2010GL046552.

Lay, T., Ye, L., Kanamori, H., Yamazaki, Y., Cheung, K. F., Kwong, K., Koper, K. D., 2013a. The October 28, 2012 Mw 7.8 Haida Gwaii underthrusting earthquake and tsunami: Slip partitioning along the Queen Charlotte Fault transpressional plate boundary. Earth Planet. Sci. Lett. 375, 57–70. doi:10.1016/j.epsl.2013.05.005.

Lay, T., Ye, L., Kanamori, H., Yamazaki, Y., Cheung, K. F., Ammon, C. J., 2013b. The February 6, 2013 Mw 8.0 Santa Cruz Islands earthquake and tsunami. Tectonophysics 608, 1109–1121. doi:10.1016/j.tecto.2013.07.001.

Madsen, P. A., Murray, R., Sørensen, O. R., 1991. A new form of the Boussinesq equations with improved linear dispersion characteristics. Coastal Eng. 15(4), 371–388. doi: 10.1016/0378-3839(91)90017-B.

Nwogu, O., 1993. Alternative form of Boussinesq equations for nearshore wave propagation. J.Waterw. Port Coast. Ocean Eng. 119(6), 618–638. doi: 10.1061/(ASCE)0733-950X(1993)119:6(618).

Newman, A. V., Hayes, G., Wei, Y., Convers, J., 2011. The 25 October 2010 Mentawai tsunami earthquake, from real-time discriminants, finite-fault rupture, and tsunami excitation. Geophys. Res. Lett. 38(5) . doi:10.1029/2010GL046498.

Okada, Y., 1992. Internal deformation due to shear and tensile faults in a half-space. Bull. Seismol. Soc. Am. 82, 1018–1040.

Peregrine, D. H., 1967. Long waves on a beach. J. fluid mech. 27(4), 815–827. doi: 10.1017/S0022112067002605.

Romano, F., Piatanesi, A., Lorito, S., D'Agostino, N., Hirata, K., Atzori, S., Yamazaki, Y., Cocco, M., 2012. Clues from joint inversion of tsunami and geodetic data of the 2011 Tohoku-oki earthquake. Sci. Rep. 2, 385. doi:10.1038/srep00385.

Romano, F., Trasatti, E., Lorito, S., Piromallo, C., Piatanesi, A., Ito, Y., Zhao, D., Hirata, K., Lanucara, P., Cocco, M., 2014. Structural control on the Tohoku earthquake rupture process investigated by 3D FEM, tsunami and geodetic data, Sci. Rep. 4, 5631. doi:10.1038/srep05631.

Saito, T., Matsuzawa, T., Obara, K., Baba, T., 2010. Dispersive tsunami of the 2010 Chile earthquake recorded by the high-sampling-rate ocean-bottom pressure gauges. Geophys. Res. Lett. 37(23). doi: 10.1029/2010GL045290.

Saito, T., Satake, K., Furumura, T., 2010. Tsunami waveform inversion including dispersive waves: the 2004 earthquake off Kii Peninsula, Japan. J. Geophys. Res. 115(B6). doi:10.1029/2009JB006884.

Saito, T., Ito, Y., Inazu, D., Hino, R., 2011. Tsunami source of the 2011 Tohoku-Oki earthquake, Japan: Inversion analysis based on dispersive tsunami simulations. Geophys. Res. Lett. 38(7). doi:10.1029/2011GL049089.

Saito, T., Inazu, D., Miyoshi, T., Hino, R., 2014. Dispersion and nonlinear effects in the 2011 Tohoku-Oki earthquake tsunami. J. Geophys. Res. Oceans 119(8), 5160–5180. doi: 10.1002/2014JC009971.

Satake, K., Nishimura, Y., Putra, P. S., Gusman, A. R., Sunendar, H., Fujii, Y., Tanioka, Y., Latief, H., Yulianto, E., 2013. Tsunami source of the 2010 Mentawai, Indonesia earthquake inferred from tsunami field survey and waveform modeling. Pure Appl. Geophys. 170, 1567–1582. doi:10.1007/s00024-012-0536-y.

Sankaranarayanan, S., Spaulding, M. L., 2003. Dispersion and stability analyses of the linearized two-dimensional shallow water equations in boundary-fitted co-ordinates. Int. J. Numer. Meth. Fluids 42(7), 741–763. doi: 10.1002/fld.552.

Shuto, N., 1991. Numerical simulation of tsunamis — Its present and near future. Nat. Hazards 4(2–3), 171–191. doi: 10.1007/BF00162786.

Singh, S. C., Hananto, N., Mukti, M., Permana, H., Djajadihardja, Y., Harjono, H., 2011. Seismic images of the megathrust rupture during the 25th October 2010 Pagai earthquake, SW Sumatra: Frontal rupture and large tsunami. Geophys. Res. Lett. 38(16). doi:10.1029/2011GL048935.

Stelling, G., Zijlema, M., 2003. An accurate and efficient finite-difference algorithm for non-hydrostatic free-surface flow with application to wave propagation. Int. J. Numer. Meth. Fluids 43(1), 1–23. doi: 10.1002/fld.595.

Smit, P., Zijlema, M., Stelling, G., 2013. Depth-induced wave breaking in a non-hydrostatic, near-shore wave model. Coastal Eng. 76, 1–16. doi: 10.1016/j.coastaleng.2013.01.008.

Titov, V. V., Synolakis, C. E., 1998. Numerical modeling of tidal wave runup. J. Waterw. Port Coast. Ocean Eng. 124(4), 157–171. doi: 10.1061/(ASCE)0733-950X(1998)124:4(157).

Tanioka, Y., Satake, K., 1996. Tsunami generation by horizontal displacement of ocean bottom. Geophys. Res. Lett. 23, 861–864. doi:10.1029/96GL00736.

Vitousek, S., Fringer, O. B., 2011. Physical vs. numerical dispersion in nonhydrostatic ocean modeling. Ocean Modell. 40(1), 72–86. doi: 10.1016/j.ocemod.2011.07.002.

Wang, X., Liu, P. L.-F., 2011. An explicit finite difference model for simulating weakly nonlinear and weakly dispersive waves over slowly varying water depth. Coastal Eng. 58(2), 173–183. doi: 10.1016/j.coastaleng.2010.09.008.

Warming, R. F., Hyett, B. J., 1974. The modified equation approach to the stability and accuracy analysis of finite-difference methods. J. Comput. Phys. 14(2), 159–179. doi: 10.1016/0021-9991(74)90011-4.

Wei, G., Kirby, J. T., 1995. Time-dependent numerical code for extended Boussinesq equations. J. Waterw. Port Coast. Ocean Eng. 121(5), 251–261. doi: 10.1061/(ASCE)0733-950X(1995)121:5(251).

Yamazaki, Y., Kowalik, Z., Cheung, K. F., 2009. Depth-integrated, non-hydrostatic model for wave breaking and run-up. Int. J. Numer. Meth. Fluids 61(5), 473–497. doi: 10.1002/fld.1952.

Yamazaki, Y., Lay, T., Cheung, K. F., Yue, H., Kanamori, H., 2011a. Modeling near-field tsunami observations to improve finite-fault slip models for the 11 March 2011 Tohoku earthquake. Geophys. Res. Lett. 38(7). doi: 10.1029/2011GL049130.

Yamazaki, Y., Cheung, K. F., Kowalik, Z., 2011b. Depth-integrated, non-hydrostatic model with grid nesting for tsunami generation, propagation, and run-up. Int. J. Numer. Meth. Fluids 67(12), 2081–2107. doi: 10.1002/fld.2485.

Yamazaki, Y., Cheung, K. F., Pawlak, G., Lay, T., 2012. Surges along the Honolulu coast from the 2011 Tohoku tsunami. Geophys. Res. Lett. 39(9). doi: 10.1029/2012GL051624.

Yamazaki, Y., Cheung, K. F., Lay, T., 2018. A Self-Consistent Fault Slip Model for the 2011 Tohoku Earthquake and Tsunami. J. Geophys. Res. Solid Earth 123(2), 1435–1458. doi: 10.1002/2017JB014749.

Yue, H., Lay, T., Li, L., Yamazaki, Y., Cheung, K. F., Rivera, L., Hill, E. M., Sieh, K., Kongko, W., Muhari, A., 2015. Validation of linearity assumptions for using tsunami waveforms in joint inversion of kinematic rupture models: Application to the 2010 Mentawai M_w 7.8 tsunami earthquake. J. Geophys. Res. Solid Earth, 120, 1728–1747. doi:10.1002/2014JB011721.

Yue, H., Lay, T., Rivera, L., Bai, Y., Yamazaki, Y., Cheung, K. F., Hill, E. M., Sieh, K., Kongko, W., Muhari, A., 2014. Rupture process of the 2010 M_w 7.8 Mentawai tsunami earthquake from joint inversion of near-field hr-GPS and teleseismic body wave recordings constrained by tsunami observations. J. Geophys. Res. Solid Earth 119, 5574–5593. doi:10.1002/2014JB011082.

Yoon, S. B., 2002. Propagation of distant tsunamis over slowly varying topography. J. Geophys. Res. Oceans 107(C10). doi: 10.1029/2001JC000791.

Zhou, H., Wei, Y., Titov, V. V., 2012. Dispersive modeling of the 2009 Samoa tsunami. Geophys. Res. Lett. 39(16). doi: 10.1029/2012GL053068.

Zijlema, M., Stelling, G., Smit, P., 2011. SWASH: An operational public domain code for simulating wave fields and rapidly varied flows in coastal waters. Coastal Eng. 58(10), 992–1012. doi: 10.1016/j.coastaleng.2011.05.015.